Precise Spatial Tuning of Visually Driven Alpha Oscillations in Human Visual Cortex

Kenichi Yuasa[1], Iris I.A. Groen[1,2], Giovanni Piantoni[3], Stephanie Montenegro[4], Adeen Flinker[4], Sasha Devore[4], Orrin Devinsky[4], Werner Doyle[4], Patricia Dugan[4], Daniel Friedman[4], Nick Ramsey[3], Natalia Petridou[3], Jonathan Winawer[1]

[1]Department of Psychology, New York University, New York, NY, USA
[2]Video & Image Sense Lab, Informatics Institute, University of Amsterdam, Amsterdam, The Netherlands
[3]University Medical Center Utrecht, Utrecht, The Netherlands
[4]New York University School of Medicine, New York, NY, USA

Abstract

Neuronal oscillations at about 10 Hz, called alpha oscillations, are often thought to arise from synchronous activity across occipital cortex, reflecting general cognitive states such as arousal and alertness. However, there is also evidence that modulation of alpha oscillations in visual cortex can be spatially specific. Here, we used intracranial electrodes in human patients to measure alpha oscillations in response to visual stimuli whose location varied systematically across the visual field. We separated the alpha oscillatory power from broadband power changes. The variation in alpha oscillatory power with stimulus position was then fit by a population receptive field (pRF) model. We find that the alpha pRFs have similar center locations to pRFs estimated from broadband power (70–180 Hz), but are several times larger. The results demonstrate that alpha suppression in human visual cortex can be precisely tuned. Finally, we show how the pattern of alpha responses can explain several features of exogenous visual attention.

Keywords: visual cortex, alpha oscillations, exogenous attention, electrocorticography (ECoG), intracranial electroencephalography (iEEG), computational models, population receptive fields

Grant support: NIH R01 MH111417 (Petridou, Winawer, Ramsey, Devinsky); JSPS Overseas Fellowship to Yuasa

The content is solely the responsibility of the authors and does not necessarily represent the official views of the National Institutes of Health

1. INTRODUCTION

Hans Berger first measured electrical oscillations at 10 Hz from the human brain using EEG [1]. Shortly thereafter, Adrian and Matthews confirmed that when a participant closes their eyes or views a uniform field, the oscillatory power increases [2]. These studies suggested that the rhythm reflects widespread neural synchrony in visual cortex, and that the presence or absence of the rhythm is likely related to overall state of the person, such as arousal or cognitive engagement. Consistent with the interpretation, subsequent studies have confirmed that global modulation of alpha oscillations can be caused by changes in arousal [3], alertness [4] or attention [5, 6].

On the other hand, several subsequent studies have found that visuospatial attention can modulate the alpha rhythm in a more localized manner. Worden et al. [7] found a reduction of the alpha oscillation in the contralateral hemisphere when attending the left or right visual fields, and an increase in the oscillation in the ipsilateral hemisphere, measured by EEG. This finding links alpha oscillations to brain areas relevant to attended visual locations, rather than to the overall state of the individual. This contralateral specificity has been replicated many times in EEG (e.g., [8, 9]). Moreover, the suppression of the alpha oscillation has been reported to be more specific than just a contralateral bias: when measuring alpha oscillations as a function of attended location, the EEG pattern differed for stimuli attended 45 deg apart within the visual same hemifield [10]. Recent studies, using either MEG or EEG in conjunction with channel encoding models [11-13], showed that modulation of the alpha rhythm was specific to cortical locations representing the polar angle of cued locations, testing between 6 and 16 polar angles.

These seemingly disparate results –some showing large-scale synchrony in the alpha rhythm and some showing spatial specificity– might be reconciled if the rhythm is generally caused by processes spanning much of the occipital cortex, but can be disrupted in small cortical regions by changes in inputs to those regions. Here, we tested the spatial specificity of the suppression of the alpha rhythm using electrocorticographic (ECoG) recordings in 9 participants using an experimental and computational approach developed for characterizing receptive fields of neural populations in fMRI [14]. This approach differs from prior work on spatial specificity because here the modulation in the alpha response is stimulus driven rather than top-down, and because the spatial specificity of the measurement (ECoG) is high. The participants viewed spatially restricted stimuli, bars containing a contrast pattern on an otherwise uniform background. We then fit a population receptive field model (pRF) to the measured alpha oscillation in each electrode in visual cortex and demonstrate that modulation of the alpha rhythm is precisely linked to stimulus location.

For comparison, we also fit a pRF model to the broadband power measured from each electrode, as in previous work [15, 16]. The broadband pRFs and alpha pRFs had similar locations (center positions) but differed in size. As expected, they also differed in sign, with the broadband signal elevated and the alpha signal suppressed by stimulus contrast in the receptive field. Together, the results suggest that the alpha oscillation in human visual cortex is spatially tuned. In the Discussion, we consider how the tuned alpha response may contribute to visual function, showing a surprisingly tight link between the spatial profiles of the stimulus-driven alpha oscillation on the one hand, and the behavioral effects of spatial attention on the other hand. Finally, we show how the former may give rise to the latter.

2. Results

2.1 Two signatures of visual responses measured with electrocorticography

Visual stimulation causes a variety of temporal response patterns measured in visual cortex. In addition to the evoked potential, which is a characteristic change in voltage time-locked to the stimulus onset, there are also spectral perturbations [17]. The largest such perturbation is the alpha oscillation. Typically, when the eyes are closed or when the participant views a blank screen (no stimulus contrast) the field potential measured from visual cortex oscillates at about 8 to 13 Hz [1]. Opening the eyes or viewing a stimulus reduces this oscillation. In addition to these spectral perturbations, there is also a broadband response, an increase in power across a wide frequency range following stimulus onset [18, 19]. Both the broadband increase and alpha suppression can be elicited by the same stimulus and measured from the same electrode. In the example shown in **Figure 1**, stimulus onset caused a broadband increase in power spanning the full range plotted, from 1 Hz to 150 Hz, and it eliminated the peak in the alpha range. The two types of response cannot be separated by simply applying filters with different temporal frequency ranges because the signals overlap in the low frequency range (6 to 22 Hz in **Figure 1D**).

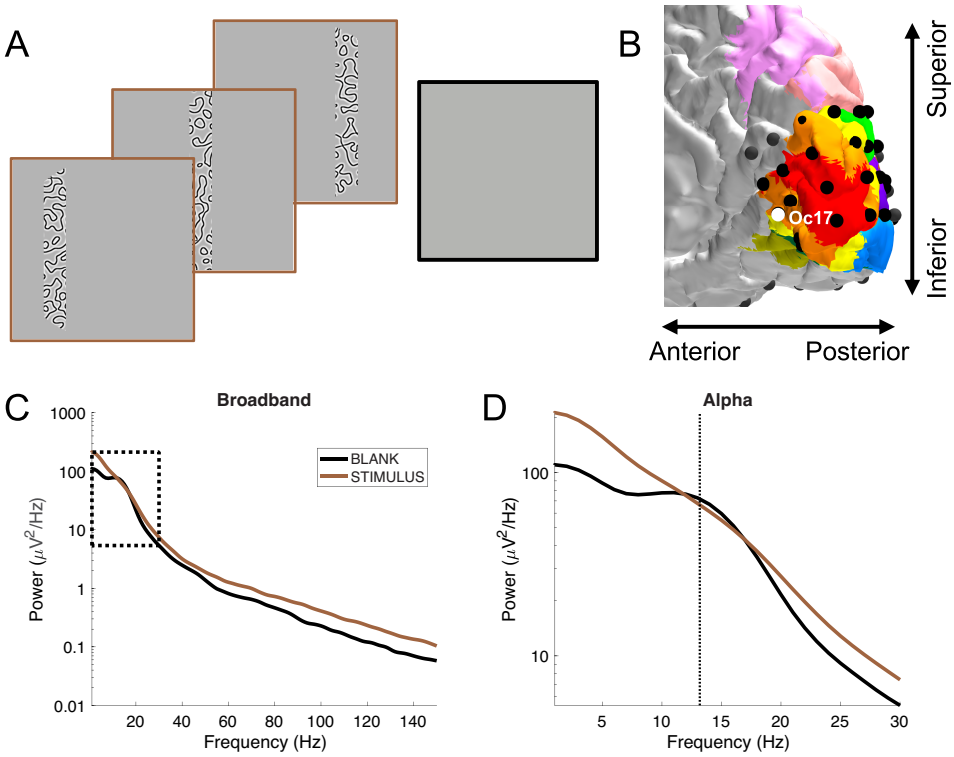

Figure 1. Two signatures of visual responses measured with ECoG. (A) Mapping stimuli. Three examples of the bar stimuli and one image of the blank stimulus during the mapping experiment (brown and black outlines, respectively). The contrast within the bar is increased here for visibility. (B) A close-up view of the right occipital cortex of Patient 2. The surface colors show several visual field maps derived from an atlas, with V1 in red, V2 in orange, and V3 in yellow. Black circles indicate ECoG electrode locations. (See **Supplementary Figure 1** for all patients) (C) The power spectral density (PSD) is shown for electrode Oc17, averaged across stimulus trials (brown) and blanks trials (black). The stimulus causes a broadband power increase, spanning frequencies from 1 Hz to 150 Hz. The dotted black rectangle indicates the frequency range shown in zoom in panel D. (D) During the blank, but not during visual stimulation, there is a peak in the spectrum at around 13 Hz (alpha oscillation, dashed vertical line). See *makeFigure1.m*.

2.2 Separating the alpha oscillation from broadband power

Because stimulus onset tends to cause an increase in broadband power and a decrease in the alpha oscillation, it is possible for the two effects to cancel at some frequencies. In the example shown in **Figure 1**, the power at the peak of the alpha oscillation (~13 Hz, black dashed line) is nearly the same during stimulus and blank. It would be incorrect, however, to infer that the alpha oscillation was unaffected by the stimulus. Rather, the decrease in the alpha oscillation and the increase in broadband power were about equal in magnitude. Depending on the relative size of these two spectral responses, the power at the alpha frequency can increase, decrease, or not change. We illustrate these possibilities with three nearby electrodes from one patient (**Figure 2**). For all three electrodes as shown in the left panels, there is a peak in the alpha range during blanks (black lines) but not during visual stimulation (brown lines). Due to the interaction with the broadband response, the power at the peak alpha frequency for stimulus relative to blank increased slightly for one electrode (Oc18), decreased slightly for a second electrode (Oc17), and decreased more substantially for a third electrode (Oc25). By adjusting the baseline to account for the broadband response as shown in the right panels, it is clear that the stimulus caused the alpha oscillation to decrease for all three electrodes. For these reasons, simply comparing the spectral power at the alpha frequency between two experimental conditions is not a good indicator of the strength of the alpha rhythm. To separate the alpha oscillation from the broadband change, we applied a baseline correction using a model-based approach.

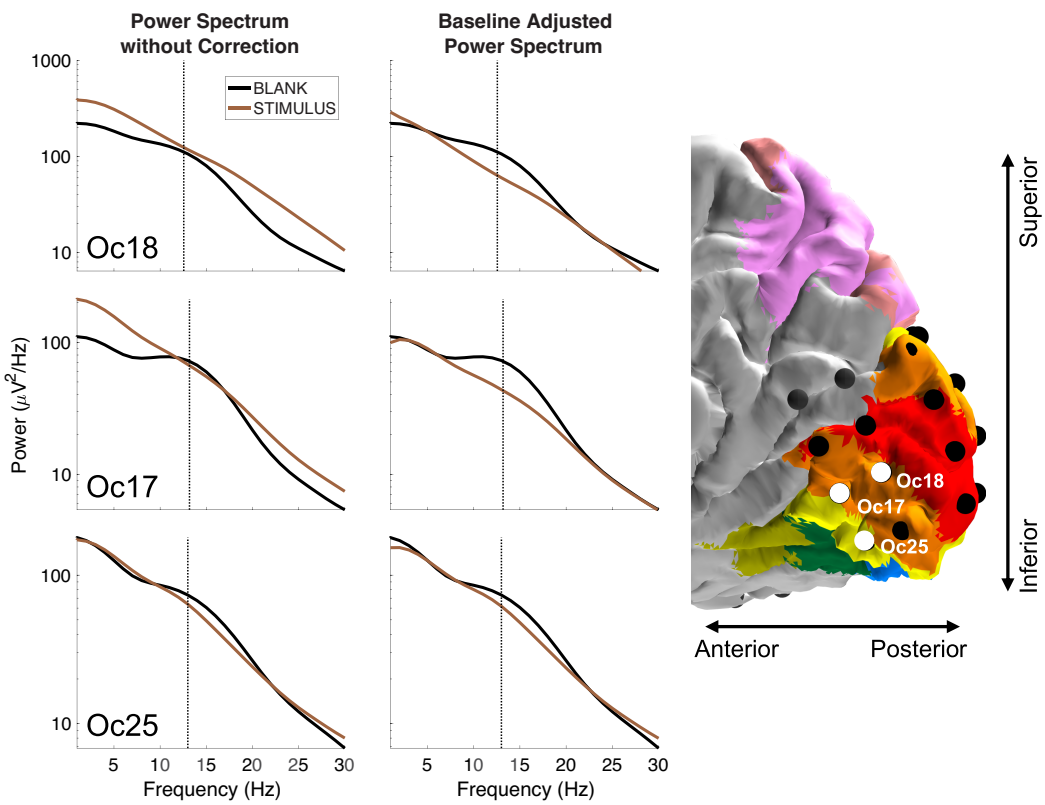

Figure 2: Interaction between the alpha rhythm and broadband power. (Left column) PSDs from 3 electrodes in Patient 2 without baseline correction show that the stimulus-related alpha power can slightly increase (Oc18), slightly decrease (Oc17) or substantially decrease (Oc25) relative to a blank stimulus. (Right column) After correcting for the broadband shift, it is clear that for all three electrodes, the alpha oscillation is suppressed by visual stimulation. The dashed vertical lines indicate the alpha peak frequency. See Methods and *makeFigure2.m*.

2.3 ALPHA RESPONSES ARE ACCURATELY PREDICTED BY A POPULATION RECEPTIVE FIELD MODEL.

By estimating the alpha oscillatory power from the low-frequency decomposition and the broadband power from the high frequency summary, we obtain two time-courses per electrode, one for the alpha suppression and one for the broadband elevation (**Figure 3**). Each point in these time courses indicates a summary measure of the response components for a 500 ms stimulus presentation. Hence the time series are at very different scales from the ms voltage time series used to derive the summary measures.

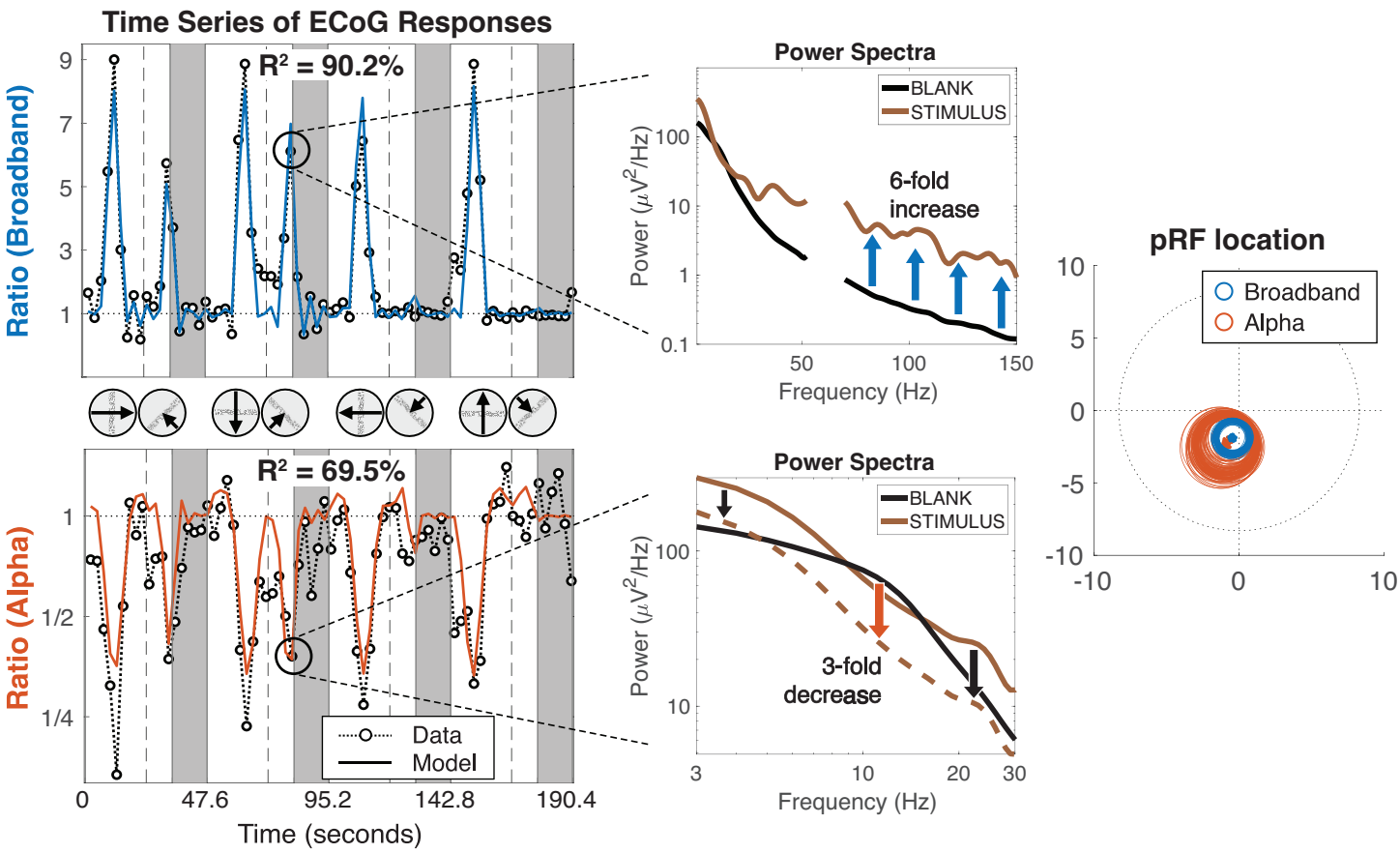

Figure 3. Example time series and pRF fits. Representative data from a V3 electrode ('GB103') from Patient 8. The left column shows the time series averaged across six 190-s mapping runs, during which bar stimuli swept the visual field 8 times (with 4 blank periods indicated by the gray bars). Each data point (black circle) is a summary value–either broadband or alpha–for one stimulus position (Equations 1-3). Predicted responses from a pRF model are shown as solid lines. The insets on the right show how the broadband and alpha summary metrics were computed for an example stimulus location. Model predictions below baseline in broadband and above baseline in alpha were possible because of the Difference of Gaussians (DoG) pRF model (see **Supplementary Figure 2)**. The rightmost panel shows the location of the pRFs fitted to the broadband and alpha times series. The circles show the 1-sigma pRF bootstrapped 100 times across the 6 repeated runs. See *makeFigure3.m*.

After a small amount of pre-processing (averaging across repeated runs, temporal decimation, dividing out the mean response during the blanks), we separately fit pRF models to the broadband and the alpha time series (**Figure 3**). The pRF model we fit assumes linear spatial summation, with a circularly symmetric Difference of Gaussians (but constrained so that the surrounding Gaussian is large compared to the field of view of the experiment). Similar results were obtained using a model with compressive spatial summation or a model in which the surround size was allowed to vary.

In the example time series, it is evident that both components of the response vary with the stimulus position: for certain stimulus locations, the broadband response increased about 5- to 10-fold over baseline and the

alpha response decreased about 3- to 5-fold. The pRF models accurately predicted these time series, with two-fold cross-validated variance explained of 90.2% for broadband and 69.5% for alpha. For both types of pRF, the center locations are in the parafovea in the left lower visual field, but the alpha pRF is about twice the size of the broadband pRF (**Figure 3**, right panel).

Next, we quantified the prediction accuracy of the pRF model fit across many electrodes, participants, and visual field maps. We first selected a large set of electrodes based only on location (see *Electrode Localization* in Methods 4.6). We then separated these electrodes into two groups based on whether or not we expected them to be visually responsive. Some of these electrodes are not expected to be visually responsive, for example if their receptive field is beyond the stimulus extent. We identified visually responsive electrodes as those whose broadband pRF model accurately predicted the broadband time course (**Supplementary Figure 3**, left). Because the broadband quantification is limited to high frequencies (70–180 Hz), this criterion provides an independent means to separate the electrodes into groups to assess the alpha pRF model accuracy, which only depends on signals below 30 Hz.

We find that for V1 to V3, the alpha pRF model explains about 37% of the cross-validated variance in the alpha time series of visually selective electrodes (**Supplementary Figure 4**). The non-visually selective electrodes provide a null distribution for comparison, and for these electrodes, the pRF model explains close to 0% of the variance. In dorsolateral maps beyond V1–V3, the alpha pRF model explained about 24% of the variance in visually responsive electrodes, and no variance in the non-responsive group. These results show that across visual cortex, the pRF models explain a substantial part of the variance in the alpha time series.

2.4 The alpha pRFs are larger than broadband pRFs, but have similar locations.

We next compared the alpha and broadband pRF parameters. We limited these comparisons to electrodes for which both signal types were well fit by pRF models (**Supplementary Figure 3**) and whose pRF centers were within the maximal stimulus extent (8.3°) for both broadband and alpha. Fifty-three electrodes met these criteria, of which 35 are assigned to V1–V3 and 45 to dorsolateral maps. (Because the assignments are probabilistic, 27 electrodes are assigned to both visual areas.)

As with the sample electrode (**Figure 3**), the center locations of the two pRF types tend to be close (**Figure 4**). However, the alpha pRFs tend to be much larger and slightly more peripheral. For most electrodes, the broadband pRFs are within the alpha pRFs. Truncating the pRF sizes at 1 standard deviation, the percentage of the broadband pRF inside the alpha pRF was 92.3% (V1–V3) and 98.0% (dorsolateral) pRFs. This overlap is not a trivial consequence of the alpha pRFs simply being large. If we shuffle the relationship between alpha and broadband pRFs across electrodes, these numbers decrease to 30.0% (V1–V3) and 25.7% (dorsolateral). We summarized the relationship between the broadband and alpha pRFs by normalizing the parameters into a common space (**Figure 4B, D**) and then averaging pRFs across electrodes for both alpha and broadband. This analysis again confirms that the broadband pRF is, on average, smaller and less peripheral than the alpha pRF, and is mostly inside the alpha pRF.

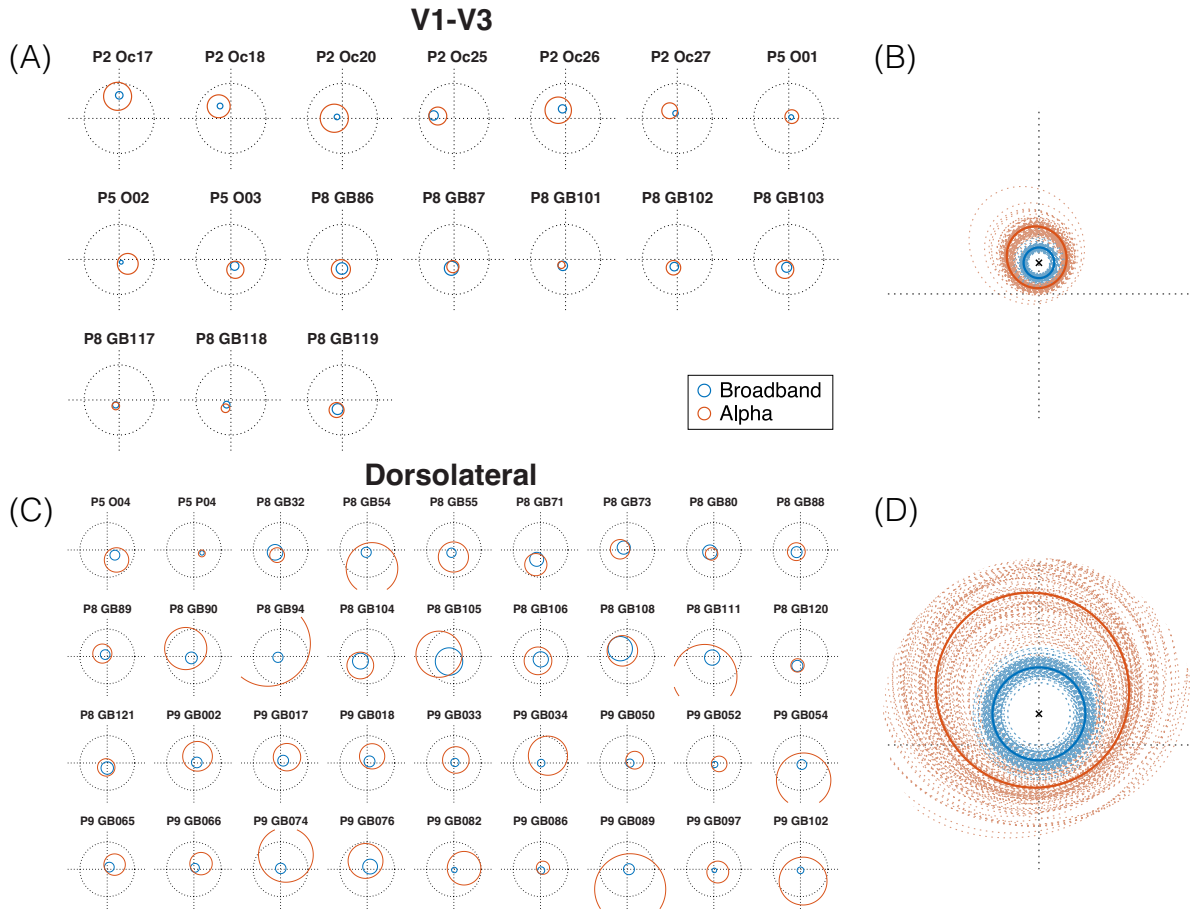

Figure 4. Alpha and broadband pRFs. For visualization purposes, each electrode was plotted only once, with the V1–V3 or dorsolateral group, even though the probabilistic assignment could have non-zero weights for both groups of maps. (We plot the electrodes with the cluster that has higher probability). (A) pRF locations in V1–V3 displayed for each electrode, as in Figure 3. (B) pRFs in V1–V3 were normalized by rotation (subtracting the broadband pRF polar angle from both the broadband and alpha pRF) and then scaling (dividing the eccentricity and size of both pRFs by the broadband pRF eccentricity). This puts the broadband pRF center at (0,1) for all electrodes, indicated by an 'x'. Within this normalized space, the average pRF across electrodes was computed 5,000 times (bootstrapping across electrodes). 100 of these averages are indicated as dotted lines, and the average across all 5,000 bootstraps is indicated as a solid line. (C,D) Same as A and B but for dorsolateral electrodes. See *makeFigure4.m*.

In addition, a direct comparison of the alpha and broadband pRFs for each separate pRF model parameter (polar angle, eccentricity, size) reveals several patterns (**Figure 5A**). First, the polar angles are highly similar between broadband and alpha both in V1–V3 and dorsolateral visual areas. Second, the eccentricities are correlated but not equal: the alpha pRFs tend to have larger eccentricities than the broadband pRFs, especially in dorsolateral visual areas. Third, the sizes of alpha pRFs also correlate with those of broadband pRFs, but are about 2–4 times larger. These results suggest that the same retinotopic maps underlie both the alpha suppression and the broadband elevation, but that the alpha suppression pools over a larger extent of visual space. In the Discussion, we speculate about why the eccentricity of the alpha pRF might be systematically larger than the broadband eccentricity, even if the two signals originate from the same retinotopic map.

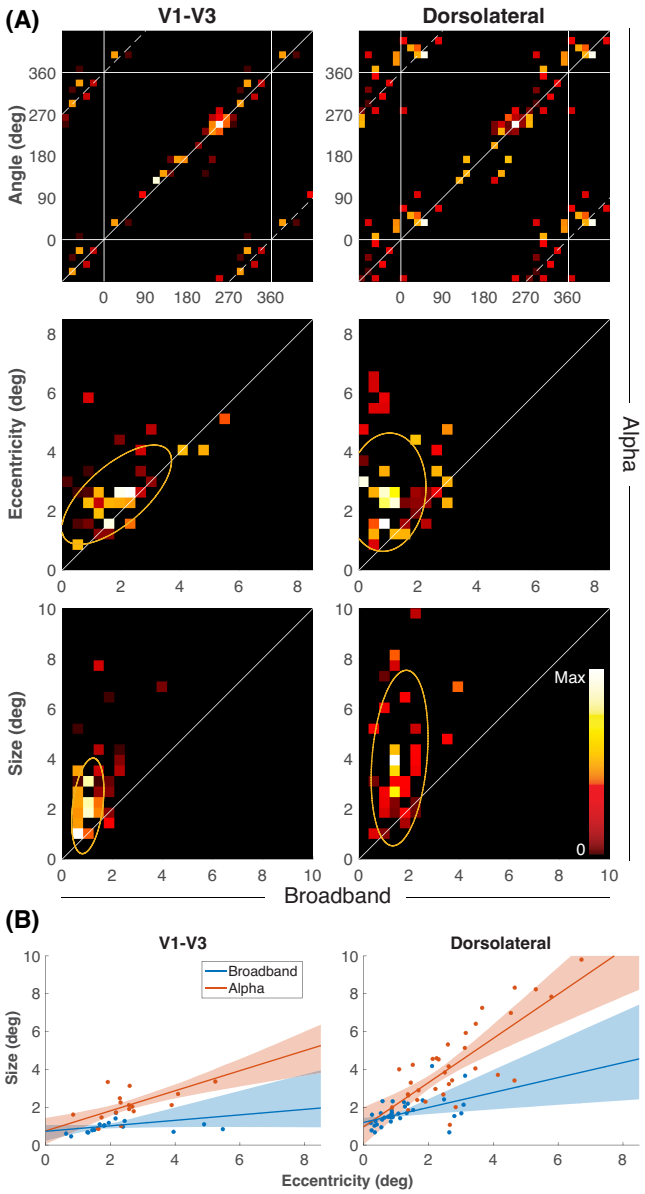

Figure 5. Correlations of alpha and broadband pRF parameters. (A) Each panel shows the relation between broadband and alpha pRF parameters in 2-D histograms. 53 electrodes were randomly sampled with replacement 5,000 times (bootstrapping), and each time they were selected they were probabilistically assigned to a visual area. The colormap indicates the frequency of pRFs in that bin (see *Comparison of alpha and broadband pRFs* in Methods 4.7). The two top panels show the relation of polar angle for V1–V3 (left) and dorsolateral retinotopic maps (right). Note that the phases in the horizontal and vertical axes are wrapped to show their circular relations. The middle and bottom panels show the relation of eccentricity and pRF sizes, respectively. Yellow ellipses indicate the 1-sd covariance ellipses. (B) Plots show pRF size vs eccentricity, both for broadband (blue) and alpha (red). As in panel A, the 53 electrodes were bootstrapped 5,000 times. The regression lines are the average across bootstraps, and the shaded regions are the 16th to 84th percentile evaluated at each eccentricity. Each electrode is plotted once, either for V1–V3 or dorsolateral maps, even though in the bootstrapping plus probabilistic assignment procedure, they could be assigned to either group. See *makeFigure5.m*.

Our results also indicate that pRF size is much larger for alpha than for broadband. Because the comparison between alpha and broadband pRF size has such a steep slope (**Figure 5A**, bottom row), one might wonder whether the size of the alpha pRFs vary in any meaningful way. Contrary to this possibility, we find that for both broadband pRFs and alpha pRFs, the pRF size systematically increases with eccentricity (**Figure 5B**), consistent with known properties of visual neurons [20] and with fMRI data [14, 21]. The slopes of the size vs. eccentricity functions are about 3 times larger for alpha than for broadband (slopes: 0.53 vs 0.15 in V1–V3; 1.17 vs 0.40 in dorsolateral, for alpha vs broadband).

2.5 The accuracy of the alpha pRFs depends on the model-based calculation

We used a model-based approach to separate the alpha oscillatory power from the broadband response because the two responses overlap in temporal frequency. Had we not used this approach, and instead used a more traditional frequency band approach –simply measuring the power in the alpha band without accounting for broadband shifts– we would have obtained different values for the alpha responses and inaccurate pRF fits. The difference between the two methods is especially clear in V1–V3, where the broadband response extends into the low frequencies (**Supplementary Figures 5 and 6**). To clarify the advantage of the model-based approach, we compared the two types of pRF fits for all visually responsive electrodes in V1–V3 (based on maximum probability of map assignment: **Figure 6**). For these comparisons, we allowed the gain to be positive or negative. First, the cross-validated variance explained was about 3 times higher for the model-based method (32%±5% vs 10%±5%, mean±sem). Second, as expected, the model-based approach consistently results in negative gain (29 out of 31 electrodes), meaning that alpha oscillations are suppressed by stimuli in the receptive field. In contrast, the frequency band approach shows a mixture of positive and negative gains (14

negative, 17 positive), complicating the interpretation. Third, the model-based method, but not the frequency band method, shows that pRF size increases with eccentricity. These analyses confirm the importance of disentangling the alpha oscillation from the broadband response.

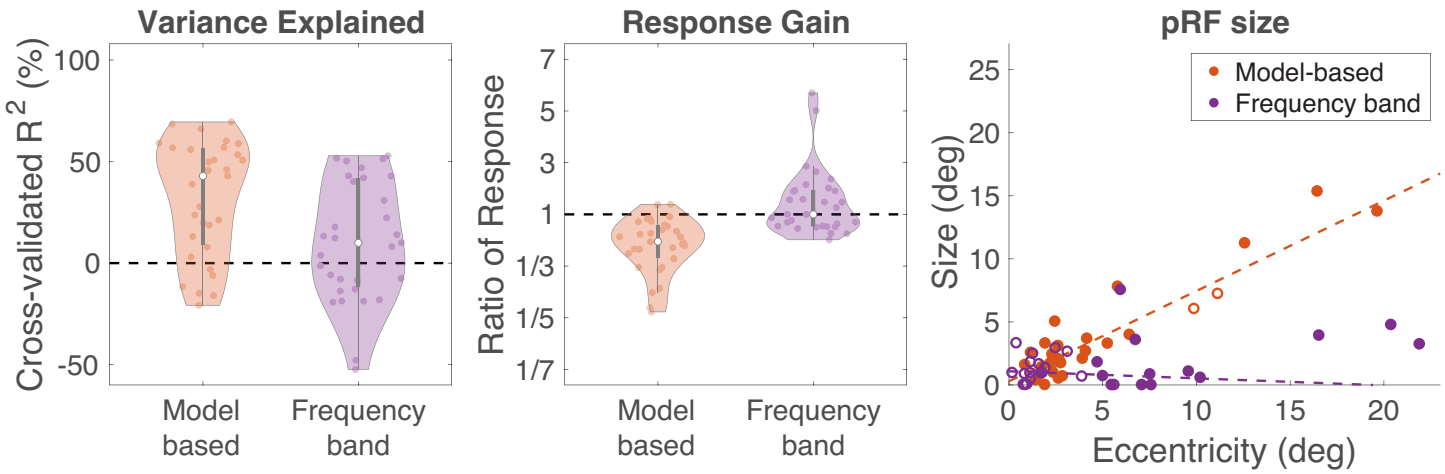

Figure 6. A comparison of model-based and frequency-band alpha pRFs. We compared pRF solutions for alpha using our spectral model ("model-based") vs by computing power within the alpha band ('frequency band"). Left: Variance explained. The white dots are the median and the gray bars are the interquartile range. Each colored dot is one electrode and the shaded regions are smoothed histograms. Middle: Response gain, plotted in the same manner as variance explained. Gain is quantified as the maximum or minimum value in the pRF fitted time series (maximal for electrodes with positive gain, minimal for electrodes with negative gain). A value above 1 means that the response increased relative to baseline (positive gain). A value below 1 means the response decreased (negative gain). Right: pRF size vs eccentricity. Electrodes are colored by the sign of the gain (filled for negative, open for positive). See *makeFigure6.m*.

2.6 Alpha oscillations are coherent across a larger spatial extent than broadband signals

The large pRFs for alpha suppression might result from a limit to the spatial resolution at which alpha oscillations can be controlled. If, for example, alpha oscillations are up- or down-regulated with a point spread function of ~5 or 10 mm of cortex, then alpha pRFs would necessarily be large. We assessed the spatial resolution of the alpha oscillation by measuring coherence of the signal across space. Specifically, we measured coherence at the alpha frequency for electrode pairs in two high-density grids (Patients 8 and 9; See **Supplementary Figure 7** for pRF parameters on the two high-density grids). These grids have 3 mm spacing between electrodes, about 10 times the density of standard grids (1 cm spacing). For comparison, we also measured the coherence between the same electrode pairs averaged across the frequencies we used for calculating broadband responses (70 Hz to 180 Hz).

We find two clear patterns as shown in **Figure 7**. First, as expected, coherence declines with distance. The alpha coherence is about 0.6 between neighboring electrodes, declining to a baseline level of about 0.35 by about 1 cm. Second, the coherence was higher at the alpha frequency than in the broadband frequencies, especially between neighboring electrodes. The pattern is the same whether the coherence is computed only from trials in which the bar position overlapped pRF, or only from trials in which it did not overlap the pRF, or both (data not shown.) Overall, the larger coherence at the alpha frequency is consistent with coarser spatial control of this signal (in mm of cortex), and larger pRFs (in deg of visual angle). The highest coherence is at the

peak alpha frequency (**Supplementary figure 8**). This suggests that the elevated coherence is not simply an artifact of greater volume conduction at low frequencies.

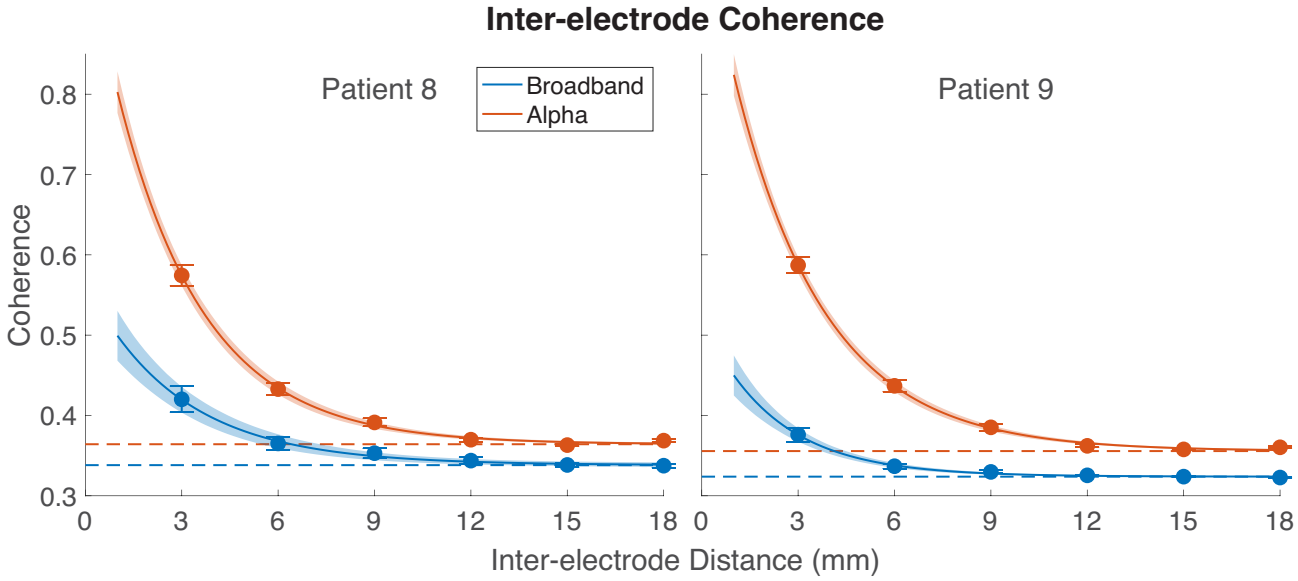

Figure 7. Inter-electrode coherence across distances in high-density grids. Coherence between electrode pairs was computed within each 1-s epoch and then averaged epochs. Seed electrodes were those which had a reliable pRF fit, and these seed electrodes were compared to all other electrodes on the grid. The curved lines indicate the average fit of an exponential decay function across 5,000 bootstraps; shading indicates 16th 84th percentile of bootstraps; dashed lines indicate the baselines the coherence converges to. See **Supplementary Figure 8** for coherence as a function of frequency. See *makeFigure7.m*.

3. Discussion

Our main two findings are that visual cortex alpha suppression is specific to stimulus location, as measured by its pRF, and that alpha pRFs are more than twice the size of broadband pRFs. This supports that alpha suppression in and near the locations of the driven response increases cortical excitability. This has implications for visual encoding in cortex, perception, and attention, with several close parallels between the alpha pRF and exogenous (stimulus-driven) attention.

3.1 What is the function of the large alpha pRFs?

The alpha oscillation was originally characterized as an "idling" or default cortical state, reflecting the absence of sensory input or task demand [1-4, 6]. However, more recent work supports the idea that alpha oscillations act as a gate, actively suppressing neural signals by reducing cortical excitability [22-26] via "pulsed inhibition" (hyperpolarization followed by rebound). This pulsed inhibition explains why cortical excitability depends on both alpha oscillation *magnitude* [7, 8, 10] and *phase* [27, 28]: when the oscillations are large, there is one phase when cortex is most excitable and one phase when it is least excitable (phase dependence), and when the oscillations are small, cortex is on average more excitable (magnitude dependence). When coupled to the large pRFs, this predicts that the onset of a focal visual stimulus will cause an increase in cortical excitability, spreading beyond the region that responds directly, i.e., with broadband field potentials and spiking (**Supplementary Figure 9**). A transient increase in excitability spreading beyond the stimulus is conceptually similar to stimulus-driven ("exogenous") spatial attention, in which a visual cue leads to faster response times, increased

discriminability, higher perceived contrast [29-31], and increased neural response, as measured by single unit spike rates [32] and BOLD fMRI [33].

The relationship may be more than conceptual, however, as we find that the spatial profiles of exogenous attention, measured behaviorally [29, 30], and of the alpha pRF are quite similar (**Figure 8**), with three close parallels. For both measures, the spatial spread (1) increases with eccentricity, (2) is asymmetric, spreading further into the periphery than toward the fovea, and (3) shows center/surround organization, with the attentional effect changing from a benefit to a cost and the alpha response changing from suppression to enhancement. The timing also matches, since exogenous attention has a maximal effect at about 100 ms [32, 34], the duration of an alpha cycle.

While many studies have proposed that attention, whether stimulus driven (exogenous) or internal (endogenous), influences the alpha oscillation [7-13], our proposal flips the causality. We propose that the stimulus causes a change in the alpha oscillation and this in turn causes increased neural responsivity and behavioral sensitivity, the hallmarks of covert spatial attention. The spatial spread of the alpha oscillation can be traced in part to the neural mechanisms generate it in the thalamus (see section *3.2*). Top-down attention may capitalize on some of the same mechanisms, as feedback to the LGN can modulate the alpha-initiating neural populations, then resulting in the same effects of cortical excitability in visual cortex that occur from bottom-up spatial processing. This is consistent with findings that endogenous attention is accompanied by local reductions in alpha oscillations [7, 9, 12].

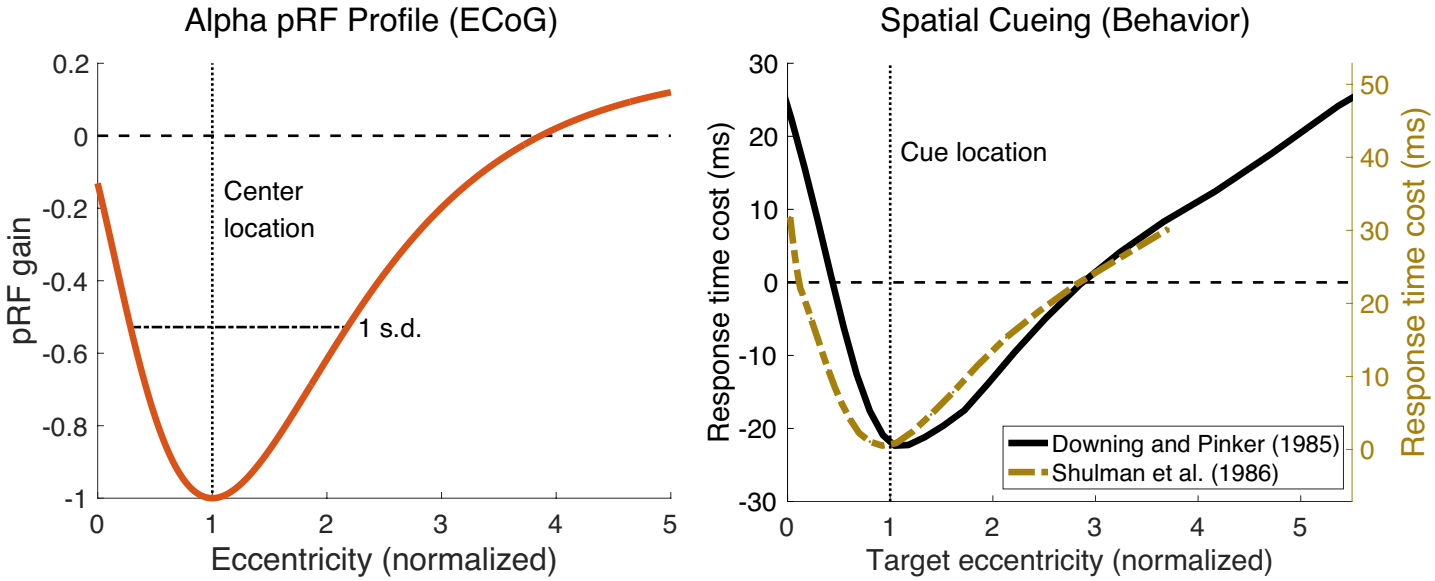

Figure 8. Asymmetric profile of alpha pRF and asymmetric effect of exogenous attention. The left panel shows an asymmetric profile of alpha pRF across normalized eccentricity in V1–V3. The right panel shows asymmetric effects of exogenous attention on normalized cue–target locations. Black line represents response time changes induced by exogenous attention from Downing and Pinker [30], relative to the response time without any attentional cue. Golden line represents response time changes induced by exogenous attention from Shulman et al. [29], relative to the response time when targets appeared at the attended locations. Results from the Shulman et al. paper with foveal cue locations at 0.5 degree eccentricity were excluded from the plot because after normalizing, the data from this condition has no overlap with the other conditions perhaps because at such a small eccentricity, a minor error in attended location makes a large difference on a normalized scale. The experimental results for each cue location are shown in **Supplementary Figure 10**. See *makeFigure8.m*.

This link to attention contrasts with the proposal that the alpha oscillation in visual cortex reflects surround suppression [15]. We think the alpha oscillation is not tightly linked to surround suppression. First, the alpha pRF

is negative, and alpha tends to be inhibitory [22-26], meaning that visual stimuli within the alpha pRF disinhibit cortex, the opposite of surround suppression. An excitatory surround (alpha suppression) and a suppressive surround can coexist if they differ in timing and feature tuning. Surround suppression is relatively fast, disappearing 60 ms after surround stimulus offset [35] whereas the ~10 Hz alpha oscillation is likely to be modulated at a slower time scale. Furthermore, surround suppression is feature-specific [35], whereas the alpha oscillation, being coherent over several mm of cortex, is unlikely to be limited only to cells whose tuning match the stimulus. Nonetheless surround suppression may be linked to neural oscillations, albeit at a higher frequency range [36, 37].

We focused on the spatial specificity of alpha oscillations on the cortical surface. A separate line of research has also examined the specificity of alpha oscillations in terms of cortical depth and inter-areal communication. One claim is that oscillations in the alpha and beta range play a role in feedback between visual areas, with evidence from nonhuman primate for specificity of alpha and beta oscillations in cortical depth [26, 38]. To our knowledge, no one has examined the spatial specificity of the alpha oscillation across the cortical surface and across cortical depth in the same study, and it remains an open question as to whether the same neural circuits are involved in both types of effects.

3.2 The importance of separating oscillatory and non-oscillatory signals

Separating the alpha power into oscillatory and broadband components was motivated by the different biological origins of the two signals. Recent work has identified a population of high threshold thalamocortical neurons that generates bursts in the alpha or theta frequency range (depending on membrane potential) [39-41]. These bursts are synchronized by gap junctions. These neurons themselves appear to be the pacemakers, generating the alpha rhythm in the LGN and transmitting it to V1. This explains the rhythmic nature of the signal (bursting), the coherence across space (synchrony by gap junctions), and the occipital locus of alpha (thalamocortical generators). The fact that this cell population is located in the LGN does not imply that the alpha oscillation is only based on feedforward signals. Feedback signals from V1 to LGN via corticothalamic cells can modulate the frequency and amplitude of the alpha generating thalamocortical cells [39]. There may also be intracortical circuits that modulate the alpha oscillation [38, 42].

The broadband response differs in several ways. First and most obvious, the signal is not limited to a narrow frequency range [16, 19, 37, 43, 44], and hence is not generally considered an oscillation [45]. Therefore, functions which are hypothesized to depend specifically on oscillations should likely not be imputed to this signal, such as a behavioral bias during certain phases of the oscillation [27, 46, 47] or long range synchronization of signals [48, 49]. Second, broadband signal are found throughout the brain [18, 45, 50], likely arising from non-oscillatory neural generators [19, 51], whereas the alpha rhythm is largest in the occipital lobe. Finally, the broadband signal measured at the electrode has lower amplitude because the generators are not synchronized across space.

The motivation to separate the signals was confirmed by the results. Compared to the frequency band method (no decomposition), the decomposition method resulted in higher variance explained, more consistent direction (negative pRFs rather than a mixture of positive and negative), and a tighter relationship between pRF eccentricity and size. The frequency band method has poorer results because it conflates two signals with different properties.

The difference between the methods likely explains some discrepancies across studies. Klink et al. [52] fit pRF models to electrode data from macaque primary visual cortex in many frequency bands, including alpha, without removing the broadband signal. They found no systematic relationship between pRF size and

eccentricity and found that the gain was positive for some electrodes and negative for others. The interpretation was that some locations in the visual field show suppression and others excitation. Our results suggest that it is more likely that most or all locations show both responses, alpha suppression and broadband increase, with either of the two signals sometimes being lager. Second, Harvey et al. [15] examined spatial selectivity of human ECoG responses in the alpha band. They fit pRF models to the broadband response and then measured alpha power for stimulus positions relative to the broadband pRFs. They reported that alpha power increased in V1 electrodes when stimuli were outside the pRF, and that there was no change in alpha power when the stimulus overlapped the broadband pRF. The combination of these two results led to an interpretation that the alpha response is specifically related to surround suppression. Our results confirm their first observation - that alpha power increases when the stimulus is outside the pRF (as reflected in our Difference of Gaussians model); however, in contrast to their report, we find strong alpha suppression when the stimulus is in the pRF center. The discrepancy is reconciled by the approach. We, too, find that total alpha power is approximately unchanged by the stimulus in the pRF center, but the model-based approach shows that this is due to cancellation from an increased broadband response and a reduced alpha oscillation, rather than to the alpha oscillation not changing.

A similar decomposition approach was used in prior ECoG studies to separate broadband power from steady state visual evoked potentials [16] and from narrowband gamma oscillations [37, 43, 44]. A generalization of this approach has also been implemented in a toolbox for separating broadband and narrowband signals [53]. These approaches are premised on the idea that different signals arise from different neurobiological causes and may be modulated independently by stimulus or task. This contrasts with the tradition of separating the field potential into frequency bands, where band-limited power is often computed without identifying a spectral peak and without removing non-oscillatory contributions.

One potential concern about our approach might be circularity: is it possible that we found the alpha and broadband signals to have opposite signs and similar pRF locations because there is in fact only one independent neural response, which we projected onto two measures? We think this is not the case. First, the broadband and the alpha power changes fitted by the pRF model were computed in different frequency ranges so that they were mathematically independent: the broadband was computed in high frequency range (70–180 Hz) and the alpha was decomposed from the low-frequency broadband response in 3–26 Hz (or 3–32 Hz). Second, if the two responses arose from one independent signal, then both the center locations and the sizes of alpha and broadband pRFs would be the same, but the alpha pRFs were much larger than the broadband pRFs.

3.3 How broad is broadband?

Since Crone et al.'s [54] observations of task related power increases at high frequency (70-100 Hz, above the typical gamma band), there has been a great deal of interest in these high frequency signals. Unlike the lower frequency gamma oscillations studied previously [55, 56], the signals above 70 Hz had no clear peak. Crone et al. speculated that this was due to the ECoG signal pooling across multiple oscillatory circuits with different peak frequencies. Signal changes above 70 Hz have been referred as "high gamma" [57-60], implicitly conveying that the signals are similar to gamma oscillations, but just at a higher frequency.

In contrast, Miller et al. [19] proposed that these signals, although appearing to be concentrated in high frequencies, do not in fact arise from neural oscillations at all. They interpreted these signals as reflecting broadband neural activity with no specific time scale, spanning the whole spectrum but obscured at lower frequencies by changes in narrowband phenomena [61]. Such task-related broadband power increases have been found in human intracranial electrodes over V1 to V3 [16] and in human microelectrode recordings of local field

potentials [18]. Our results confirm their findings as the broadband increase is observed from as low as 3 Hz in V1–V3. The broadband responses in low-frequency (3–26 Hz) and high-frequency band (70–180 Hz) showed similar response patterns to the pRF stimuli, as reflected in similar pRF model parameters, suggesting they have a common cause.

There may, however, be variability across cortical locations (and across people) in the neural circuit properties that generate broadband responses. We find a difference in the pattern between V1–V3 and the dorsolateral maps. In V1–V3, the stimulus-related broadband elevation is clear all the way down to 3 Hz or lower, whereas in dorsolateral cortex it is clear only down to about 25 Hz. The difference could reflect fundamental differences in the type of field potentials that can be generated from the two regions, or could depend on how well matched the stimuli are to the tuning of the brain areas: the simple contrast patterns used for pRF mapping more effectively drive the early visual field maps than higher level areas (e.g., producing twice the percent signal change in high broadband signals). The human microelectrode recordings [18] indicate that broadband power extending as low as 2 Hz can be measured across many brain regions, including frontal, parietal, and occipital cortices as well as hippocampus and amygdala. A further consideration is that broadband power changes might entail changes in the exponent of the spectral power function in addition to a change in the scaling [53]. In either case, however, it is likely that the power changes in high frequency regions reported here and elsewhere (e.g., [45]) reflect processes which are not oscillatory and hence not limited to a narrow range of frequencies. And because the model-based method of quantifying alpha oscillations shows a clear advantage for some regions (V1–V3) and no disadvantage for others, it is a more interpretable and general method than simply measuring the power at a particular frequency.

3.4 Conclusion

With high spatial precision measurements, we have discovered that spectral power changes in the alpha range reflect both suppression of alpha oscillations and elevation of broadband power. Separating the two responses was essential for accurately fitting pRF models to the alpha oscillation. The large, negative alpha pRF indicates that visual stimulation suppresses alpha oscillations and likely increases cortical excitability over a large cortical extent (larger than the region with broadband and spiking increases). Together, these results predict many of the effects observed in spatial cueing experiments, thus providing further links between the alpha oscillation and spatial attention. More generally, alpha oscillation is likely to play a role in how cortex encodes sensory information.

REFERENCES

1. Berger, H. Über das Elektrenkephalogramm des Menschen. *Archiv für Psychiatrie und Nervenkrankheiten* **87**, 527-570 (1929).
2. Adrian, E.D. & Matthews, B.H. The Berger rhythm: potential changes from the occipital lobes in man. *Brain : a journal of neurology* **57**, 355-385 (1934).
3. Barry, R.J., Clarke, A.R., Johnstone, S.J., Magee, C.A. & Rushby, J.A. EEG differences between eyes-closed and eyes-open resting conditions. *Clinical Neurophysiology* **118**, 2765-2773 (2007).
4. Matousek, M. & Petersen, I. A method for assessing alertness fluctuations from EEG spectra. *Electroencephalogr Clin Neurophysiol* **55**, 108-113 (1983).
5. Foxe, J.J., Simpson, G.V. & Ahlfors, S.P. Parieto - occipital ~1 0Hz activity reflects anticipatory state of visual attention mechanisms. *NeuroReport* **9**, 3929-3933 (1998).
6. Klimesch, W., Doppelmayr, M., Russegger, H., Pachinger, T. & Schwaiger, J. Induced alpha band power changes in the human EEG and attention. *Neurosci Lett* **244**, 73-76 (1998).
7. Worden, M.S., Foxe, J.J., Wang, N. & Simpson, G.V. Anticipatory Biasing of Visuospatial Attention Indexed by Retinotopically Specific α-Bank Electroencephalography Increases over Occipital Cortex. *The Journal of Neuroscience* **20**, RC63-RC63 (2000).
8. Kelly, S.P., Lalor, E.C., Reilly, R.B. & Foxe, J.J. Increases in alpha oscillatory power reflect an active retinotopic mechanism for distracter suppression during sustained visuospatial attention. *J Neurophysiol* **95**, 3844-3851 (2006).
9. Sauseng, P., *et al.* A shift of visual spatial attention is selectively associated with human EEG alpha activity. *European Journal of Neuroscience* **22**, 2917-2926 (2005).
10. Rihs, T.A., Michel, C.M. & Thut, G. Mechanisms of selective inhibition in visual spatial attention are indexed by alpha-band EEG synchronization. *The European journal of neuroscience* **25**, 603-610 (2007).
11. Foster, J.J., Sutterer, D.W., Serences, J.T., Vogel, E.K. & Awh, E. Alpha-Band Oscillations Enable Spatially and Temporally Resolved Tracking of Covert Spatial Attention. *Psychol Sci* **28**, 929-941 (2017).
12. Popov, T., Gips, B., Kastner, S. & Jensen, O. Spatial specificity of alpha oscillations in the human visual system. *Hum Brain Mapp* **40**, 4432-4440 (2019).
13. Samaha, J., Sprague, T.C. & Postle, B.R. Decoding and Reconstructing the Focus of Spatial Attention from the Topography of Alpha-band Oscillations. *J Cogn Neurosci* **28**, 1090-1097 (2016).
14. Dumoulin, S.O. & Wandell, B.A. Population receptive field estimates in human visual cortex. *NeuroImage* **39**, 647-660 (2008).
15. Harvey, B.M., *et al.* Frequency specific spatial interactions in human electrocorticography: V1 alpha oscillations reflect surround suppression. *NeuroImage* **65**, 424-432 (2013).
16. Winawer, J., *et al.* Asynchronous broadband signals are the principal source of the BOLD response in human visual cortex. *Current biology : CB* **23**, 1145-1153 (2013).
17. Makeig, S. Auditory event-related dynamics of the EEG spectrum and effects of exposure to tones. *Electroencephalogr Clin Neurophysiol* **86**, 283-293 (1993).
18. Manning, J.R., Jacobs, J., Fried, I. & Kahana, M.J. Broadband shifts in local field potential power spectra are correlated with single-neuron spiking in humans. *The Journal of neuroscience : the official journal of the Society for Neuroscience* **29**, 13613-13620 (2009).
19. Miller, K.J., Sorensen, L.B., Ojemann, J.G. & den Nijs, M. Power-law scaling in the brain surface electric potential. *Plos Comput Biol* **5**, e1000609 (2009).
20. Newsome, W.T., Maunsell, J.H. & Van Essen, D.C. Ventral posterior visual area of the macaque: visual topography and areal boundaries. *J Comp Neurol* **252**, 139-153 (1986).
21. Kay, K.N., Winawer, J., Mezer, A. & Wandell, B.A. Compressive spatial summation in human visual cortex. *J Neurophysiol* **110**, 481-494 (2013).
22. Jensen, O. & Mazaheri, A. Shaping functional architecture by oscillatory alpha activity: gating by inhibition. *Frontiers in human neuroscience* **4**, 186 (2010).
23. Klimesch, W., Sauseng, P. & Hanslmayr, S. EEG alpha oscillations: the inhibition-timing hypothesis. *Brain Res Rev* **53**, 63-88 (2007).
24. Mazaheri, A. & Jensen, O. Rhythmic pulsing: linking ongoing brain activity with evoked responses. *Frontiers in human neuroscience* **4**, 177 (2010).
25. Van Diepen, R.M., Foxe, J.J. & Mazaheri, A. The functional role of alpha-band activity in attentional processing: the current zeitgeist and future outlook. *Curr Opin Psychol* **29**, 229-238 (2019).
26. Bastos, A.M., Lundqvist, M., Waite, A.S., Kopell, N. & Miller, E.K. Layer and rhythm specificity for predictive routing. *Proceedings of the National Academy of Sciences of the United States of America* **117**, 31459-31469 (2020).
27. Spaak, E., de Lange, F.P. & Jensen, O. Local entrainment of alpha oscillations by visual stimuli causes cyclic modulation of perception. *The Journal of neuroscience : the official journal of the Society for Neuroscience* **34**, 3536-3544 (2014).
28. Osipova, D., Hermes, D. & Jensen, O. Gamma power is phase-locked to posterior alpha activity. *PLoS One* **3**, e3990 (2008).
29. Shulman, G.L., Sheehy, J.B. & Wilson, J. Gradients of spatial attention. *Acta Psychol (Amst)* **61**, 167-181 (1986).
30. Downing, C.J. & Pinker, S. The spatial structure of visual attention. in *Mechanisms of attention: Attention and performance XI* 171-187 (1985).
31. Carrasco, M. Visual attention: the past 25 years. *Vision research* **51**, 1484-1525 (2011).
32. Wang, F., Chen, M., Yan, Y., Zhaoping, L. & Li, W. Modulation of Neuronal Responses by Exogenous Attention in Macaque Primary Visual Cortex. *The Journal of neuroscience : the official journal of the Society for Neuroscience* **35**, 13419-13429 (2015).
33. Dugue, L., Merriam, E.P., Heeger, D.J. & Carrasco, M. Differential impact of endogenous and exogenous attention on activity in human visual cortex. *Sci Rep* **10**, 21274 (2020).

34. Nakayama, K. & Mackeben, M. Sustained and transient components of focal visual attention. *Vision research* **29**, 1631-1647 (1989).
35. Bair, W., Cavanaugh, J.R. & Movshon, J.A. Time course and time-distance relationships for surround suppression in macaque V1 neurons. *The Journal of neuroscience : the official journal of the Society for Neuroscience* **23**, 7690-7701 (2003).
36. Ray, S., Ni, A.M. & Maunsell, J.H. Strength of gamma rhythm depends on normalization. *Plos Biol* **11**, e1001477 (2013).
37. Hermes, D., Petridou, N., Kay, K.N. & Winawer, J. An image-computable model for the stimulus selectivity of gamma oscillations. *Elife* **8**, 583567 (2019).
38. Bollimunta, A., Mo, J., Schroeder, C.E. & Ding, M. Neuronal mechanisms and attentional modulation of corticothalamic alpha oscillations. *The Journal of neuroscience : the official journal of the Society for Neuroscience* **31**, 4935-4943 (2011).
39. Hughes, S.W. & Crunelli, V. Just a phase they're going through: the complex interaction of intrinsic high-threshold bursting and gap junctions in the generation of thalamic alpha and theta rhythms. *Int J Psychophysiol* **64**, 3-17 (2007).
40. Hughes, S.W., *et al.* Thalamic Gap Junctions Control Local Neuronal Synchrony and Influence Macroscopic Oscillation Amplitude during EEG Alpha Rhythms. *Front Psychol* **2**, 193 (2011).
41. Lorincz, M.L., Kekesi, K.A., Juhasz, G., Crunelli, V. & Hughes, S.W. Temporal framing of thalamic relay-mode firing by phasic inhibition during the alpha rhythm. *Neuron* **63**, 683-696 (2009).
42. Clayton, M.S., Yeung, N. & Cohen Kadosh, R. The many characters of visual alpha oscillations. *The European journal of neuroscience* **48**, 2498-2508 (2018).
43. Hermes, D., Miller, K.J., Wandell, B.A. & Winawer, J. Stimulus Dependence of Gamma Oscillations in Human Visual Cortex. *Cereb Cortex* **25**, 2951-2959 (2015).
44. Hermes, D., Nguyen, M. & Winawer, J. Neuronal synchrony and the relation between the blood-oxygen-level dependent response and the local field potential. *Plos Biol* **15** (2017).
45. Miller, K.J., *et al.* Broadband changes in the cortical surface potential track activation of functionally diverse neuronal populations. *NeuroImage* **85**, 711-720 (2014).
46. Mathewson, K.E., Gratton, G., Fabiani, M., Beck, D.M. & Ro, T. To See or Not to See: Prestimulus alpha Phase Predicts Visual Awareness. *Journal of Neuroscience* **29**, 2725-2732 (2009).
47. Busch, N.A., Dubois, J. & VanRullen, R. The phase of ongoing EEG oscillations predicts visual perception. *The Journal of neuroscience : the official journal of the Society for Neuroscience* **29**, 7869-7876 (2009).
48. Palva, S. & Palva, J.M. Functional roles of alpha-band phase synchronization in local and large-scale cortical networks. *Front Psychol* **2**, 204 (2011).
49. Palva, S. & Palva, J.M. Discovering oscillatory interaction networks with M/EEG: challenges and breakthroughs. *Trends in cognitive sciences* **16**, 219-230 (2012).
50. Kupers, E.R., *et al.* A non-invasive, quantitative study of broadband spectral responses in human visual cortex. *PLoS One* **13**, e0193107 (2018).
51. Bedard, C., Kroger, H. & Destexhe, A. Does the 1/f frequency scaling of brain signals reflect self-organized critical states? *Phys Rev Lett* **97**, 118102 (2006).
52. Klink, P.C., Chen, X., Vanduffel, W. & Roelfsema, P.R. Population receptive fields in nonhuman primates from whole-brain fMRI and large-scale neurophysiology in visual cortex. *Elife* **10** (2021).
53. Donoghue, T., *et al.* Parameterizing neural power spectra into periodic and aperiodic components. *Nat Neurosci* **23**, 1655-1665 (2020).
54. Crone, N.E., Miglioretti, D.L., Gordon, B. & Lesser, R.P. Functional mapping of human sensorimotor cortex with electrocorticographic spectral analysis. II. Event-related synchronization in the gamma band. *Brain : a journal of neurology* **121 (Pt 12)**, 2301-2315 (1998).
55. Eckhorn, R., *et al.* Coherent oscillations: a mechanism of feature linking in the visual cortex? Multiple electrode and correlation analyses in the cat. *Biological cybernetics* **60**, 121-130 (1988).
56. Gray, C.M. & Singer, W. Stimulus-specific neuronal oscillations in orientation columns of cat visual cortex. *Proceedings of the National Academy of Sciences of the United States of America* **86**, 1698-1702 (1989).
57. Brovelli, A., Lachaux, J.P., Kahane, P. & Boussaoud, D. High gamma frequency oscillatory activity dissociates attention from intention in the human premotor cortex. *NeuroImage* **28**, 154-164 (2005).
58. Canolty, R.T., *et al.* High gamma power is phase-locked to theta oscillations in human neocortex. *Science* **313**, 1626-1628 (2006).
59. Ray, S. & Maunsell, J.H. Different origins of gamma rhythm and high-gamma activity in macaque visual cortex. *Plos Biol* **9**, e1000610 (2011).
60. Bartoli, E., *et al.* Functionally Distinct Gamma Range Activity Revealed by Stimulus Tuning in Human Visual Cortex. *Current biology : CB* **29**, 3345-3358 e3347 (2019).
61. Miller, K.J., Zanos, S., Fetz, E.E., den Nijs, M. & Ojemann, J.G. Decoupling the cortical power spectrum reveals real-time representation of individual finger movements in humans. *The Journal of neuroscience : the official journal of the Society for Neuroscience* **29**, 3132-3137 (2009).

4. METHODS

The dataset was collected as part of a larger project funded by the NIH (R01MH111417). The methods for collecting and preprocessing the visual ECoG data have been described recently [62]. For convenience, data collection methods below duplicate some of the text from the methods section of Groen et al. [62] with occasional modifications to reflect slight differences in participants, electrode selection, and pre-processing.

4.1 DATA AND CODE AVAILABILITY

All data and code are freely available. We list the main sources of data and code here for convenience: The data are shared in BIDS format via Open Neuro (https://openneuro.org/datasets/ds004194). The analysis depends on two repositories with MATLAB code: one for conversion to BIDS and pre-processing (ECoG_utils, https://github.com/WinawerLab/ECoG_utils), and one for analysis of the pre-processed data (ECoG_alphaPRF, https://github.com/KenYMB/ECoG_alphaPRF). The analysis also has several dependencies on existing public tools, including analyzePRF [21] (https://github.com/cvnlab/analyzePRF), FieldTrip [63] (https://github.com/fieldtrip/fieldtrip), and FreeSurfer (http://freesurfer.net). Within the main analysis toolbox for this paper (ECoG_alphaPRF), there is a MATLAB script to re-generate each of the main data figures in this paper, called '*makeFigure1.m*', '*makeFigure2.m*', etc. Sharing both the raw data and the full set of software tools for analysis and visualization facilitates computational reproducibility and enables inspection of computational methods to a level of detail that is not possible from a standard written Methods section alone.

All code used for generating the stimuli and for experimental stimulus presentation can be found at https://github.com/BAIRR01/BAIR_stimuli and https://github.com/BAIRR01/vistadisp.

4.2 PARTICIPANTS

ECoG data were recorded from 9 participants implanted with subdural electrodes for clinical purposes. Data from 7 patients were collected at New York University Grossman School of Medicine (NYU), and from 2 patients at the University Medical Center Utrecht (UMCU). The participants gave informed consent to participate, and the study was approved by the NYU Grossman School of Medicine Institutional Review Board and the ethical committee of the UMCU. Detailed information about each participant and their implantation is provided in **Table 1**. Two patients (p03 and p04) were not included because they did not participate in the pRF experiment which we analyzed for the purpose of the current study.

Patient	BIDS Code	Age	Sex	Site	PRF runs	Hemi	Implantation	Coverage	# of Visual	Matching areas with maximum probability
Patient 1	p01	30	F	UMCU	4	L	strip, depth	lat-occ, lat-par, vent-temp	8	PHC, V3AB, LO, TO
Patient 2	p02	18	F	UMCU	2	R	grid, strip	med-occ, lat-occ, lat-temp, vent-temp	20	V1, V2, V3, hV4, V3AB, TO, IPS
Patient 3	p05	31	F	NYU	4	R	2× grid, strip, depth	lat-occ, lat-par, frontal, ant-temp	21	V2, V3, hV4, LO, TO, IPS
Patient 4	p06	19	F	NYU	2	L	grid, strip, depth	med-occ, lat-occ, lat-par, ant-temp, frontal	28	V1, V2, V3, hV4, V3AB, LO, TO, IPS
Patient 5	p07	41	F	NYU	4	L	grid, strip, depth	lat-occ, lat-par, med-occ, ant-temp, frontal	20	V1, V2, V3, V3AB, TO, IPS
Patient 6	p08	47	F	NYU	2	R	grid, strip, depth	lat-par, ant-temp	6	LO, TO, IPS
Patient 7	p09	25	M	NYU	4	L,R	bilateral grid, strip, depth	lat-occ, lat-par	8	LO, TO, IPS
Patient 8	p10	23	M	NYU	6	R	grid, HD grid, strip, depth	lat-occ, lat-par, post-vent	130	V2, V3, V3AB, LO, TO, IPS, SPL
Patient 9	p11	19	F	NYU	6	L	grid, HD grid, strip, depth	lat-occ, lat-par, post-vent	93	hV4, VO, V3AB, LO, TO, IPS

Table 1. Overview of patient data included in this dataset. The patient number and subject code for BIDS do not always match because the 9 subjects with pRF data are a subset of 11 subjects from a larger BIDS dataset (https://openneuro.org/datasets/ds004194). Two of the 11 patients did not take part in pRF experiments.

4.3 ECoG RECORDINGS

NYU

Stimuli were shown on a 15 in. MacBook Pro laptop. The laptop was placed 50 cm from the participant's eyes at chest level. Screen resolution was 1280 × 800 pixels (33 × 21 cm). Prior to the start of the experiment, the screen luminance was linearized using a lookup table based on spectrophotometer measurements (Cambridge Research Systems). ECoG data were recorded using four kinds of electrodes: Standard size grids, linear strips, depth electrodes, and high-density grids, with the following details.

- Standard grids (8 × 8 arrays) and strips (4 to 12 contact linear strips) were implanted, consisting of subdural platinum-iridium electrodes embedded in flexible silicone sheets. The electrodes had 2.3-mm diameter exposed surface and 10-mm center-to-center spacing (Ad-Tech Medical Instrument, Racine, Wisconsin, USA).
- Penetrating depth electrodes (1 × 8 or 1 × 12 contacts) were implanted, consisting of 1.1-mm diameter electrodes, 5- to 10-mm center-to-center spacing (Ad-Tech Medical Instrument).
- In two patients (Patient 8 and 9), there were small, high-density grids (16 x 8 array) implanted over lateral posterior occipital cortex. These high-density grids were comprised of electrodes with 1-mm diameter exposed surface and 3-mm center-to-center spacing (PMT Corporation, Chanhassen, Minnesota, USA).

Recordings were made using one of two amplifier types: NicoletOne amplifier (Natus Neurologics, Middleton, WI), bandpass filtered from 0.16-250 Hz and digitized at 512 Hz, and Neuroworks Quantum Amplifier (Natus Biomedical, Appleton, WI) recorded at 2048 Hz, bandpass filtered at 0.01–682.67 Hz and then downsampled to 512 Hz. Stimulus onsets were recorded along with the ECoG data using an audio cable connecting the laptop and the ECoG amplifier. Behavioral responses were recorded using a Macintosh wired external numeric keypad that was placed in a comfortable position for the participant (usually their lap) and connected to the laptop through a USB port. Participants self-initiated the start of the next experiment by pushing a designated response button on the number pad.

UMCU

Stimuli were shown on an NEC MultiSync® E221N LCD monitor positioned 75 cm from the participant's eyes. Screen resolution was 1920 x 1080 pixels (48 x 27cm). Stimulus onsets were recorded along with the ECoG data using a serial port that connected the laptop to the ECoG amplifier. As no spectrophotometer was available at the UMCU, screen luminance was linearized using the built-in gamma table of the display device. Data were recorded using the same kinds of electrodes as NYU: Standard grids and strips, and depth electrodes, and using a MicroMed amplifier (MicroMed, Treviso, Italy) at 2048 Hz with a low-pass filter of 0.15Hz and a high-pass filter of 500Hz. Responses were recorded with a custom-made response pad.

4.4 pRF Stimulus

Visual stimuli were generated in MATLAB 2018b. Stimuli were shown at 8.3 degrees of visual angle (16.6 degrees stimulus diameter) using Psychtoolbox-3 (http://psychtoolbox.org/) and were presented at a frame rate of 60 Hz. Custom code was developed in order to equalize visual stimulation across the two recording sites as much as possible; for example, all stimuli were constructed at high resolution (2000 x 2000 pixels) and subsequently downsampled in a site-specific manner such that the stimulus was displayed at the same visual angle at both recording sites (see *stimMakePRFExperiment.m* and *bairExperimentSpecs.m* in BAIRR01/BAIR_stimuli). Stimuli consisted of grayscale bandpass noise patterns that were created following procedures outlined in Kay et al. [21]. Briefly, the pattern stimuli were created by low-pass filtering white noise, thresholding the result, performing edge detection, inverting the image polarity such that the edges are black, and applying a band-pass filter centered at 3 cycles per degree (see *createPatternStimulus.m*).

All stimuli were presented within bar apertures; the remainder of the display was filled with neutral gray. This stimulus has been shown to effectively elicit responses in most retinotopic areas [64]. The width of the bar aperture was 2 degrees of visual angle, which was 12.5% of the full stimulus extent. The bar aperture swept across the visual field in eight directions consisting of twenty-eight discrete steps per sweep, 850 ms step duration. During each step, the bar stimulus was displayed for 500 ms followed by a 350 ms blank period showing a gray mean luminance image. The eight sweeps included 2 horizontal (left to right or right to left), 2 vertical (up to down or down to up) and 4 diagonal sweeps (starting from one of the 4 directions). For the diagonal sweeps, the bar was replaced with a blank for the last 16 of the 28 steps, so that the stimuli swept diagonally across the visual field from one side to the center in twelve steps followed by 13.6 s of blanks (16 x 850 ms). Each experiment included 224 850-ms steps plus 3 s of blank at the beginning and end, for a total of 196.4 seconds.

4.5 Experimental procedure

All participants completed pRF mapping experiments in which they viewed visual stimuli for the purpose of estimating the spatial selectivity for individual electrodes (population receptive field mapping [14]). In these experiments, participants were instructed to fixate on a cross located in the center of the screen and press a button every time the cross changed color (from green to red or red to green). Fixation cross color changes were created independently from the stimulus sequence and occurred at randomly chosen intervals ranging between 1 and 5 s. Participants completed one to three recording sessions. Each session included two pRF mapping experiments. The experimenter stayed in the room throughout the testing session. Participants were encouraged to take short breaks between experiments.

4.6 ECoG data analysis

Preprocessing

Data were preprocessed using MATLAB 2020b with custom scripts available at https://github.com/WinawerLab/ECoG_utils (see *Data and Code Availability* for access to data and computational methods to reproduce all analyses). Raw data traces obtained in each recording session were visually inspected for spiking, drift or other artifacts. Electrodes that showed large artifacts or showed epileptic activity were marked as bad and excluded from analysis. Data were then separated into individual experiments and formatted to conform to the iEEG-BIDS format [65]. Data for each experiment were re-referenced to the common average across electrodes for that experiment, whereby a separate common average was calculated per electrode group (i.e., separate common average for each of the 4 electrode types–standard grid, high-density grid, strip, and depth electrodes, see *bidsEcogRereference.m*). The re-referenced voltage time series for each experiment were written to BIDS derivatives directories.

Electrode localization

Intracranial electrode arrays from NYU patients were localized from the post-implantation structural T1-weighted MRI images and co-registered to the preoperative T1-weighted MRI [66]. Electrodes from UMCU patients were localized from the postoperative CT scan and co-registered to the preoperative T1-weighted MRI [67]. Electrode coordinates were computed in native T1 space and visualized on the pial surface reconstruction of the preoperative T1-weighted scan generated using FreeSurfer.

Cortical visual field maps were generated for each individual participant based on the T1-weighted scan by aligning the surface topology with a probabilistically defined retinotopic atlas derived from a retinotopic fMRI mapping dataset as shown in **Supplementary Figure 1** [68]. We use the full probability map, rather than the maximum probability map, in order to account for the uncertainty in the mapping between electrodes location and visual field map in the patient's native T1 space. For each cortical vertex, the atlas contains the probability of being assigned to each of 25 maps. Electrodes were matched to the probabilistic atlases using the following procedure (see *bidsEcogMatchElectrodesToAtlas.m* in ECoG_utils): For each electrode, the distance to all the nodes in the FreeSurfer pial surface mesh was calculated, and the node with the smallest distance was determined to be the matching node. The atlas value for the matching node was then used to assign the electrode to a probability of belonging to each of the following visual areas: V1v, V1d, V2v, V2d, V3v, V3d, hV4, VO1, VO2, PHC1, PHC2, TO2, TO1, LO2, LO1, V3b, V3a, IPS0, IPS1, IPS2, IPS3, IPS4, IPS5, SPL1, or FEF. We then merged these 25 visual areas into 12 groups: V1 (V1v + V1d), V2 (V2v + V2d), V3 (V3v + V3d), hV4, VO

(VO1 + VO2), PHC (PHC1 + PHC2), TO (TO1 + TO2), LO (LO1 + LO2), V3AB (V3a + V3b), IPS (IPS0–5), SPL (SPL1), or FEF.

To visualize the electrodes on the cortical surface we use a modified version of the Wang et al. full probability atlas. First, we select vertices that have a probability greater than 95% of not belonging to any of the retinotopic regions, and labeled as "none". Next, for the remaining vertices we assigned the region with the highest probability, even if the probability for not belonging to one of the retinotopic regions was higher (e.g., **Figures 1**, **2**, **Supplementary Figures 1, and 7**).

Data epoching

The preprocessed data were analyzed using custom MATLAB code (https://github.com/KenYMB/ECoG_alphaPRF). First, a dataset was created by reading in the voltage time courses of each experiment for each participant from the corresponding BIDS derivatives folders. To combine the UMCU and NYU participants into a single dataset, the UMCU data were downsampled at 512 Hz to match the sample rate of the NYU data. Visual inspection of the data indicated an obvious delay in response onset for the UMCU participants relative to the NYU participants. The cause of the delay could not be tracked down but it was clearly artifactual. To correct the delay, UMCU data were aligned to the NYU data based on a cross-correlation on the average event-related potentials (ERPs) across all stimulus conditions from the V1 and V2 electrodes from three participants (1 UMCU, 2 NYU). The delay in stimulus presentation was estimated to be 72ms, and stimulus onsets of the UMCU participants were shifted accordingly (Groen et al. 2022). One NYU patient (Patient 3) had inaccurate trigger onset signals for each stimulus event due to a recording malfunction. The onset timings for this patient were reconstructed by using the first onset in each experiment (which were recorded correctly), and then assumed to begin every 850 ms as controlled by the stimulus computer.

The voltage data were then epoched for all trials between [-0.2 and 0.8] seconds relative to stimulus onset (see *ecog_prf_getData.m*). Baseline-correction was applied by subtracting the average pre-stimulus amplitude computed in [-0.2 and 0] seconds within each trial.

Electrode selection and exclusion of noisy data

In two participants (10 and 11), there were high-density grids over lateral posterior cortex. All electrodes from these two grids were included in the pRF analyses (described below). In addition, we also included all standard grid or strip electrodes which were assigned to one of the visual areas with a minimum of 5% according to the Wang et al full probability atlas. Together, this resulted in 239 high-density electrodes and 131 standard grid or strip electrodes. After excluding 4 electrodes due to high noise (see paragraph below), the data selection resulted in a total of 366 electrodes from 9 participants. Of these 366 electrodes, 334 covered visual areas V1, V2, V3, hV4, VO, PHC, TO, LO, V3AB, IPS, and SPL. The other 32 electrodes belonged to one of the high-density grids but could not be assigned to a particular visual area.

Furthermore, we excluded epochs containing voltages that were large relative to the evoked signal. Specifically, for each electrode, we derived a distribution of the expected peak of the evoked signal by (1) converting voltage to power (squared voltage), (2) taking the maximum power from each epoch, excluding blanks, during the stimulus period (0–500 ms), and (3) fitting an inverse Gaussian distribution to these numbers. This yields one distribution for each electrode. Next, we computed the evoked potential by averaging the voltage time series across all epochs excluding blanks, and projected this out from every epoch. Finally, from the residual time series in each epoch, we compared the maximum power to the inverse Gaussian distribution for that electrode. If that value fell in the far tail, defined as the upper 0.01% of the area under the curve, then we excluded that

epoch. This resulted in the exclusion of 0.8% of epochs (3,422 out of ~430,000). Twelve electrodes showed unusually high variance across trials (over three standard deviations across electrodes) and were therefore excluded from further analysis. Furthermore, two runs from Patient 3 were not included in final analyses, as the patient broke fixation during these runs (see *ecog_prf_selectData.m*).

Computing power spectral density

We computed power spectral density (PSD) for each electrode in each epoch. We assumed in our analysis that the alpha oscillation is bandpass, centered at about 8–13 Hz, and that the biophysical processes giving rise to the oscillation are distinct from those causing the low-pass visually evoked potential. The two signals overlap in frequency, however. Hence, in order to remove the influence of the evoked signal on estimates of alpha power (and other spectral responses) [43, 44], we computed the voltage signal averaged across trials ("Event related potential", or ERP) separately for epochs with stimulus presentation and for epochs without stimuli (blanks). We then regressed the ERP time series out from each epoch (see *ecog_prf_regressData.m*). From the time series after removal of the ERP, we computed the PSD during the stimulus presentation period (0–500 ms) in 1 Hz bins. We used Welch's (1967) method with a 200 ms length Hann window with 50% overlap to attenuate edge effects. Baseline power spectra were computed for each electrode by taking a geometric average of the power spectra at each frequency bin across blank epochs (see *ecog_prf_spectra.m*).

4.7 pRF ANALYSIS

Each participant had multiple identical pRF runs, with the same sequence of 224 trials per run, and 2 to 6 runs per participant. For each electrode and for each of the 224 trials, we computed the geometric mean of the PSD per frequency bin across the repeated runs, to yield a sequence of 224 PSDs per electrode. We extracted a summary measure of alpha power and broadband power from each of the PSDs, so that for each electrode, we obtained a series of 224 alpha values and 224 broadband values.

Estimating alpha power from the PSD

We used a model-based approach to compute the alpha responses. This is important because the broadband response extends to low frequencies, and if one just measured the power in a pre-defined range of frequencies corresponding to the alpha band, it would reflect a sum of the two signals rather than the alpha response alone.

To decompose the spectral power into a broadband shift and a change in the alpha oscillation, we modeled the spectral power changes in the 3 to 26 Hz range as the sum of two responses in the log power / log frequency domain: a linear shift to capture the broadband response and a Gaussian to capture the alpha response (**Figure 9**), according to the formula based on Hermes et al. [43] decomposition of broadband and gamma oscillations:

$$Stimulus\ evoked\ change\ in\ power = \quad Broadband\ elevation \quad + \quad Alpha\ suppression$$

$$\log_{10}\left(\frac{P_S(k)}{P_B(k)}\right) \quad = (\beta_{broadband_low} - n(k-\mu)) \ + \ \beta_{alpha}\, G(k|\mu,\sigma),$$

$$k = \log_{10}(frequency),$$

$$G(k|\mu,\sigma) = e^{\frac{-(k-\mu)^2}{2\sigma^2}},$$

with $8\ Hz < 10^{\mu} < 13\ Hz$. **[Equation 1]**

$P(k)$ is the power spectral density (PSD), either for the stimulus (P_S) or the blank (P_B). 10^{μ} indicates the peak alpha frequency. We define the change in power as the logarithm of the ratio, so that, for example, a doubling or halving in power are treated symmetrically. Typically, the response to a stimulus is an increase in broadband power and a decrease in the alpha oscillation, so $\beta_{broadband_low}$ is usually positive and β_{alpha} is usually negative. We refer to the broadband component as $\beta_{broadband_low}$ to distinguish it from the broadband power we estimate at higher frequencies (70–180 Hz). While the two responses might result from a common biological cause, as proposed by [19], we treat the power elevation at lower and higher frequencies separately here. This ensures that the pRFs estimated from the broadband response (70–180 Hz) and from the alpha responses are independent measures, and that any relationship between them is not an artifact of the decomposition method. Confining the broadband signal to higher frequencies to estimate the broadband pRFs also facilitates comparison with other reports, since most groups exclude low frequencies from their estimates of ECoG broadband data. Hence the term $\beta_{broadband_low}$ is defined here only to help estimate the alpha response, and is not used directly for fitting pRF models in our main analysis comparing alpha and broadband pRFs.

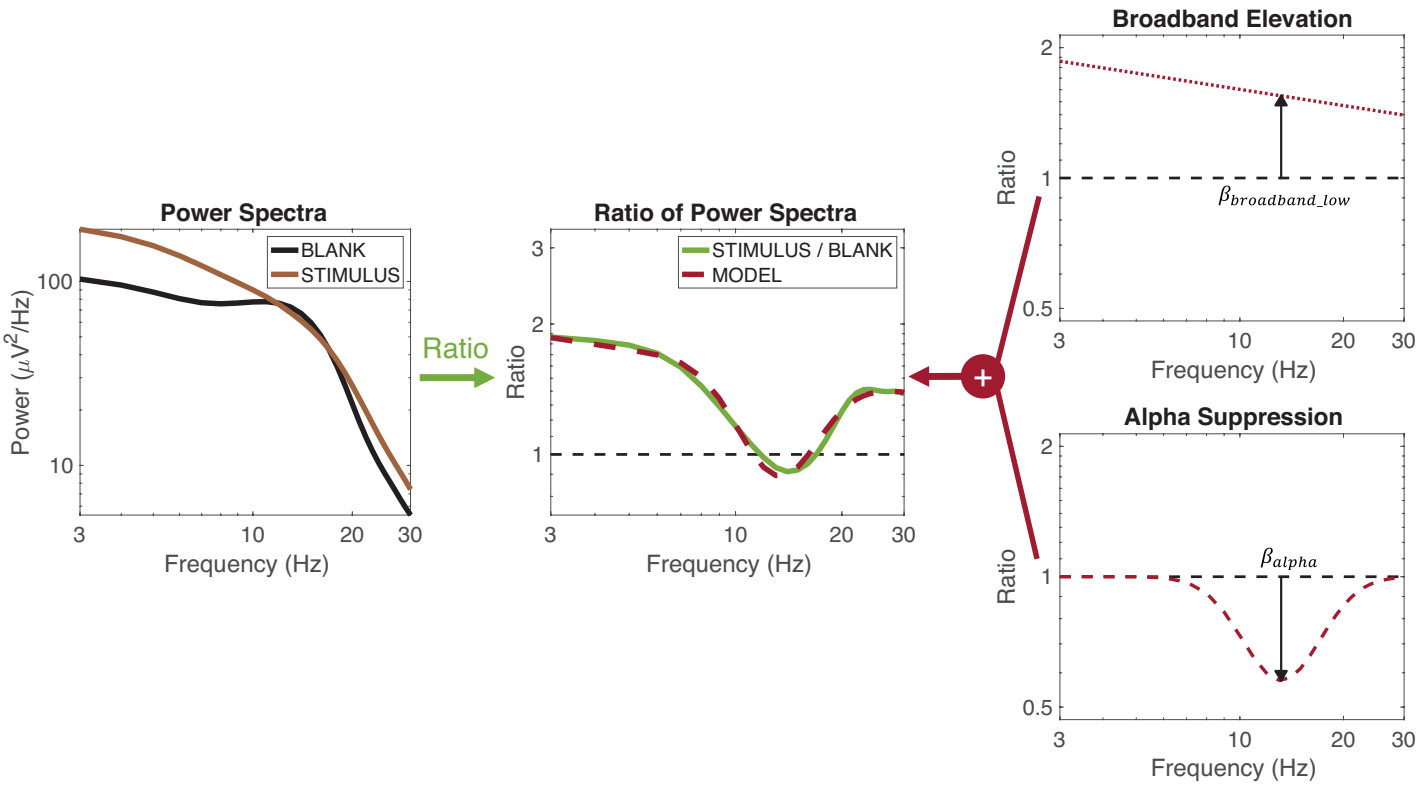

Figure 9. Schematics of model-based alpha computation. The left panel shows the average power spectra elicited by the pRF mapping stimuli (brown) and blanks (black) from a representative electrode. The middle panel shows the ratio between the two power spectra (green). This ratio, evaluated on log-log axes, is modeled (dashed red) as the sum of a broadband elevation (right panel, top) and an alpha suppression (right panel, bottom). The magnitude of alpha suppression is the coefficient of the Gaussian bump (β_{alpha}, black arrow). See **Equation 1** and *makeFigure9.m*.

For two participants, there was a prominent spectral peak just above the alpha band (~24 Hz, beta band), which interfered with this spectral decomposition. In this case, we added a third component to the model, identical to the term for alpha, except with a center constrained to 15–30 Hz instead of 8 to 13 Hz, and applied the model in the 3 to 32 Hz range:

$$\log_{10}\left(\frac{P_S(k)}{P_B(k)}\right) = (\beta_{broadband_low} - n(k-\mu_1)) + \beta_{alpha}\, G(k|\mu_1,\sigma_1) + \beta_{beta}\, G(k|\mu_2,\sigma_2),$$

$$k = \log_{10}(frequency),$$

$$G(k|\mu_1,\sigma_1) = e^{\frac{-(k-\mu_1)^2}{2{\sigma_1}^2}},\ G(k|\mu_2,\sigma_2) = e^{\frac{-(k-\mu_2)^2}{2{\sigma_2}^2}},$$

with $8\ Hz < 10^{\mu_1} < 13\ Hz$ and $15\ Hz < 10^{\mu_2} < 30\ Hz$. **[Equation 2]**

The amplitude of this beta oscillation was modeled as a nuisance variable in that it helped improve our estimate of the alpha oscillation but was not used further in analysis. Including this additional term for the other participants had negligible effect, since there were not clear beta oscillations in other participants so that the coefficient was usually close to 0. For simplicity, we omitted the beta terms for all datasets except for the two participants which required it. This spectral decomposition was computed for each aperture step in the pRF experiments with the constraint that the peak alpha frequency, 10^{μ}, was within ±1 Hz of the peak estimated from averaging across the responses to all apertures for each electrode.

Estimating broadband power from the PSD

Separately, we estimated the broadband power elevation in the higher frequency range (70–180 Hz) for each electrode and each stimulus location. The broadband power elevation was defined as the ratio of stimulus power (P_S) to blank power (P_B), where power was computed as the geometric mean across frequencies from 70 to 180 Hz in 1-Hz bins, according to the formula:

$$Broadband\ elevation = \beta_{broadband} = \frac{geometric\ mean\ (P_S(f))}{geometric\ mean\ (P_B(f))},$$

with $70\ Hz < f < 180\ Hz$ (excluding harmonics of line noise). **[Equation 3]**

The harmonics of power line components were excluded from the averaging: 116–125 and 176–180 Hz from NYU patients and 96–105 and 146–155 Hz from UMCU patients.

Time courses from pRF analyses

The computations above yield one estimate of alpha power and one estimate of broadband power per trial per electrode, meaning two time series with 224 samples. Visual inspection showed that these two metrics both tended to rise and fall relatively slowly relative to the small changes in position of the sweeping bar aperture. Therefore, the rapid fluctuations in the summary time series were mostly noise. To increase signal-to-noise ratio, each time course was decimated using a lowpass Chebyshev Type I infinite impulse response (IIR) filter of order 3, resulting in 75 time points (see *ecog_prf_fitalpha.m* and *ecog_prf_constructTimeSeries.m*). The same decimation procedure was applied to the binary contrast aperture time series.

Fitting pRF models

The alpha and broadband power time course and the sequential stimulus contrast apertures were used to estimate two pRFs per electrode (one for alpha, one for broadband), using a Difference of Gaussians (DoG) model [69]. The DoG model predicts the response amplitude as the dot product of the binarized stimulus aperture and a pRF. For broadband, the pRF was assumed to be a positive 2D Gaussian (circular) summed with a negative surround. For alpha, the pRF was assumed to be negative with a positive surround. Early analyses indicated a need for the surround, but a lack of precision in estimating its size. For simplicity and to avoid

overfitting, we assumed the surround to extend infinitely. Hence the pRF is a Gaussian with an offset. For each model (alpha and broadband) for each electrode, 5 parameters were fit: center location of the pRF (x, y), standard deviation of the center Gaussian (σ), and the gains of the center (g_1) and the surround (g_2). We estimated these pRF parameters using the analyzePRF toolbox [21]. We modified the toolbox to incorporate the surround (see *analyzePRFdog.m* in ECoG_utils). The predicted response is obtained by the dot product of aperture and pRF:

$$RESP = STIM \cdot PRF,$$

$$RESP = STIM \cdot (g_1 \cdot G_1(x, y, \sigma) - g_2).$$

[Equation 4]

We optimized the parameters $(x, y, \sigma, g_1, and\ g_2)$ across all stimulus locations by maximizing the coefficient of determination (R^2) between the 75 predicted time points and observed time series using a least squares non-linear search solver (*lsqcurvefit*), employing the levenberg-marquardt algorithm:

$$R^2 = 1 - \frac{\sum_{stimuli}(RESP_{MODEL} - RESP_{DATA})^2}{\sum_{stimuli} RESP_{DATA}{}^2}.$$

[Equation 5]

We set the boundary on the center of Gaussian (x, y) as [-16.6° and 16.6°], two times the maximal extent of the visual stimulus. We performed the fitting twice, once to compute pRF parameters and once to compute model accuracy separately. We use the results of the fit to the complete dataset for each electrode to report pRF parameters. To estimate model accuracy, we fit the data using two-fold cross-validation. For cross-validation, each time course was separated into first and second half time courses. Both halves included all horizontal and vertical stimulus positions but reversed in temporal order. We estimated the pRF parameters from each half time course (37 or 38 time points), and used these parameters to predict the response to the other half of the time course. Then we obtained the cross-validated coefficient of determination as the model accuracy of the concatenated predictions (R^2):

$$cross\text{-}validated\ R^2 = 1 - \frac{\sum(RESP_{cross\text{-}validated\ MODEL} - RESP_{DATA})^2}{\sum RESP_{DATA}{}^2}.$$

[Equation 6]

To summarize the data from each electrode, we took the cross-validated variance explained from the split half analysis, and the parameter estimates from the full fit, converting the x and y parameters to polar angle and eccentricity (see *ecog_prf_analyzePRF.m*).

Comparison of alpha and broadband pRFs

We compared the pRF parameters for the alpha model and broadband models for a subset of electrodes which showed reasonably good fits for each of the two measures. To be included in the comparison, electrodes needed to have a pRF center within the maximal stimulus extent (8.3°) for both broadband and alpha, and to have a goodness of fit exceeding thresholds for both broadband and alpha.

The goodness of fit thresholds were defined based on null distributions. The null distributions were computed separately for broadband and alpha. In each case, we shuffled the assignment of pRF parameters to electrodes,

computing how accurately the pRF model from one electrode explained the time series from a different electrode. We did this 5,000 times to compute a distribution, and chose a variance explained threshold that was higher than 95% of the values in this null distribution. That value was 31% for broadband and 22% for alpha (**Supplementary Figure 3**). Electrodes whose cross-validated variance explained without shuffling exceeded these values were included for the comparison between the two types of signals (assuming their pRF centers were within the 8.3° stimulus aperture).

This procedure resulted in 54 electrodes from 4 patients. Of these, 35 electrodes had non-zero probability assignments to V1, V2, or V3, 45 to dorsolateral visual areas (TO, LO, V3AB, or IPS), and 3 to ventral visual areas (hV4, VO, or PHC). The total is greater than 54 because of the probabilistic assignment of electrodes to areas (See *Electrode localization* for the probabilistic assignment). See **Table 2** for details.

	Visual area	**# of electrodes**	**Contributing patients (# of electrodes)**
Electrodes in visual areas (Figures S2, S3)	V1–V3	104	1 (1), 2 (15), 3 (6), 4 (13), 5 (6), 8 (54), 9 (9)
	Dorsolateral	303	1 (7), 2 (7), 3 (18), 4 (19), 5 (18), 6 (6), 7 (8), 8 (130), 9 (90)
	Total	329	1 (7), 2 (19), 3 (21), 4 (28), 5 (20), 6 (6), 7 (8), 8 (130), 9 (90)
Visually responsive electrodes (Figures 6, S4)	V1–V3	55	1 (1), 2 (9), 5 (6), 8 (32), 9 (7)
	Dorsolateral	121	1 (1), 2 (2), 3 (1), 4 (1), 5 (4), 7 (1), 8 (63), 9 (48)
	Total	131	1 (1), 2 (10), 3 (1), 4 (1), 5 (6), 7 (1), 8 (63), 9 (48)
Electrodes for comparing broadband and alpha pRFs (Figures 4, 5, S5, S6)	V1–V3	35	2 (6), 5 (5), 8 (20), 9 (4)
	Dorsolateral	45	5 (3), 8 (25), 9 (17)
	Total	53	2 (6), 5 (5), 8 (25), 9 (17)

Table 2. Overview of electrodes and patients per visual area and figure. The totals are lower than the sum of V1–V3 and Dorsolateral because some electrodes are counted toward both (see *Electrode Localization*, section 4.6). The electrodes in visual areas indicate electrodes which have at least 5% probability to be assigned to a visual area. The visually responsive electrodes indicate the electrodes in visual areas with satisfying thresholding criteria in broadband pRFs. The electrodes for comparing broadband and alpha pRFs are the electrodes satisfying thresholding criteria both in broadband and alpha pRFs. Because assignments to the visual areas are probabilistic, the total numbers of electrodes are less than the sum of the numbers of electrodes in each visual area.

To summarize the relationship between broadband and alpha pRF parameters separately for low (V1–V3) vs. high (dorsolateral) visual areas, we used a resampling procedure that accounts for uncertainty of the assignment between electrodes and visual area. We sampled from the 54 electrodes 54 times with replacement, and randomly assigned each electrode to a visual area according to the Wang full probability distributions. After the resampling, average 17.7 electrodes were assigned to V1–V3, 23.2 to dorsolateral, and 53 to either (i.e., one electrode was not assigned to either of V1–V3 or dorsolateral). We repeated this procedure 5,000 times. We then plotted pRF parameters from the broadband and alpha models as 2D histograms (e.g., **Figure 5 and Supplementary Figure 6**). For the 2D histograms, we computed and plotted 68% confidence intervals derived from the covariance matrix using the function *error_ellipse.m* (https://www.mathworks.com/matlabcentral/fileexchange/4705-error_ellipse).

4.8 Coherence analysis

Coherence in the high-density grids

We assessed the spatial dependence of coherence in each of the two signals (broadband and alpha) by analyzing data from the two high-density grids (Patients 8 and 9). For each pair of electrodes on a grid, we computed the cross power spectral density (CPSD) in each epoch. The CPSD was computed on the time series after regressing out the ERPs, as described above (*Computing power spectral density*) in 500-ms sliding windows (75% overlap, Hann windows, Welch's method [70]). Regressing out the ERPs ensures that coherence measured between electrodes is not a result of the two electrodes having similar stimulus-triggered responses. The CPSD was calculated over the stimulus interval (-200–800 ms) in 1 Hz frequency bins (see *ecog_prf_crossspectra.m*). For each electrode pair, and for each of the 224 time series, the magnitude-squared coherence (MSC) was computed and averaged across the N repeated experiments:

$$MSC_{xy}(f) = \frac{1}{N}\sum_{runs}^{N} \frac{P_{xy}(f)\, P_{xy}^{*}(f)}{P_x(f)\, P_y(f)},$$

where P_{xy} is the CPSD across two electrodes, and P_x, P_y are the PSDs at each electrode. **[Equation 7]**

This calculation returns an array of time series by frequency bins for each electrode pair. We then derived summary metrics of coherence for alpha and broadband (see *ecog_prf_connectivity.m*). We defined the alpha coherence between a seed electrode and all other electrodes on the high-density grid as the coherence at the peak alpha frequency. We defined broadband coherence as the average of the coherence in the broadband frequency range, 70–180 Hz. For every electrode pair on a grid, we then had 224 measures of alpha coherence and 224 measures of broadband coherence. For consistency with the pRF analyses, these time series of alpha and broadband coherence were again decimated into 75 time points.

We then binned the coherence data by electrode pair as a function of inter-electrode distance and by trial as a function of stimulus location. Electrode pairs were binned into inter-electrode distances in multiples of 3 mm. Only electrodes pairs for which the seed electrode satisfied the pRF threshold as computed in the previous section were selected (see *Comparison of alpha and broadband pRFs*). We used bootstrapping to compute error bars. For each inter-electrode distance, we randomly sampled electrode pairs with replacement, and averaged the coherence across the electrode pairs and trials. We repeated this procedure 5,000 times. The averaged coherences were fitted to the exponential decay function across inter-electrode distances using the least squares method.

Acknowledgments

We thank **Dora Hermes** (Mayo Clinic) for help on the model-based method to analyze alpha oscillations, and for feedback on an earlier version of the work; **Mike Landy** (NYU) for suggesting we compare the spatial spread of attentional cueing with the spatial spread of the alpha pRF; **Kaoru Amano** (U Tokyo) and his lab for providing feedback on an early version of the work; **Ilona Bloem** (NYU) for feedback on the manuscript; and **Hiromasa Takemura** (NIPS, Japan) for providing feedback on the project.

REFERENCES

14. Dumoulin, S.O. & Wandell, B.A. Population receptive field estimates in human visual cortex. *NeuroImage* **39**, 647-660 (2008).
19. Miller, K.J., Sorensen, L.B., Ojemann, J.G. & den Nijs, M. Power-law scaling in the brain surface electric potential. *Plos Comput Biol* **5**, e1000609 (2009).
21. Kay, K.N., Winawer, J., Mezer, A. & Wandell, B.A. Compressive spatial summation in human visual cortex. *J Neurophysiol* **110**, 481-494 (2013).
43. Hermes, D., Miller, K.J., Wandell, B.A. & Winawer, J. Stimulus Dependence of Gamma Oscillations in Human Visual Cortex. *Cereb Cortex* **25**, 2951-2959 (2015).
44. Hermes, D., Nguyen, M. & Winawer, J. Neuronal synchrony and the relation between the blood-oxygen-level dependent response and the local field potential. *Plos Biol* **15** (2017).
62. Groen, I.I.A.*, et al.* Temporal dynamics of neural responses in human visual cortex. *The Journal of neuroscience : the official journal of the Society for Neuroscience* **42**, 7562-7580 (2022).
63. Oostenveld, R., Fries, P., Maris, E. & Schoffelen, J.M. FieldTrip: Open source software for advanced analysis of MEG, EEG, and invasive electrophysiological data. *Computational intelligence and neuroscience* **2011**, 156869 (2011).
64. Kay, K.N., Winawer, J., Rokem, A., Mezer, A. & Wandell, B.A. A two-stage cascade model of BOLD responses in human visual cortex. *Plos Comput Biol* **9**, e1003079 (2013).
65. Holdgraf, C.*, et al.* iEEG-BIDS, extending the Brain Imaging Data Structure specification to human intracranial electrophysiology. *Sci Data* **6**, 102 (2019).
66. Yang, A.I.*, et al.* Localization of dense intracranial electrode arrays using magnetic resonance imaging. *NeuroImage* **63**, 157-165 (2012).
67. Hermes, D., Miller, K.J., Noordmans, H.J., Vansteensel, M.J. & Ramsey, N.F. Automated electrocorticographic electrode localization on individually rendered brain surfaces. *J Neurosci Methods* **185**, 293-298 (2010).
68. Wang, L., Mruczek, R.E., Arcaro, M.J. & Kastner, S. Probabilistic Maps of Visual Topography in Human Cortex. *Cereb Cortex* **25**, 3911-3931 (2015).
69. Zuiderbaan, W., Harvey, B.M. & Dumoulin, S.O. Modeling center-surround configurations in population receptive fields using fMRI. *Journal of vision* **12**, 10 (2012).
70. Welch, P. The use of fast Fourier transform for the estimation of power spectra: A method based on time averaging over short, modified periodograms. *IEEE Transactions on Audio and Electroacoustics* **15**, 70-73 (1967).

Supplementary Figures

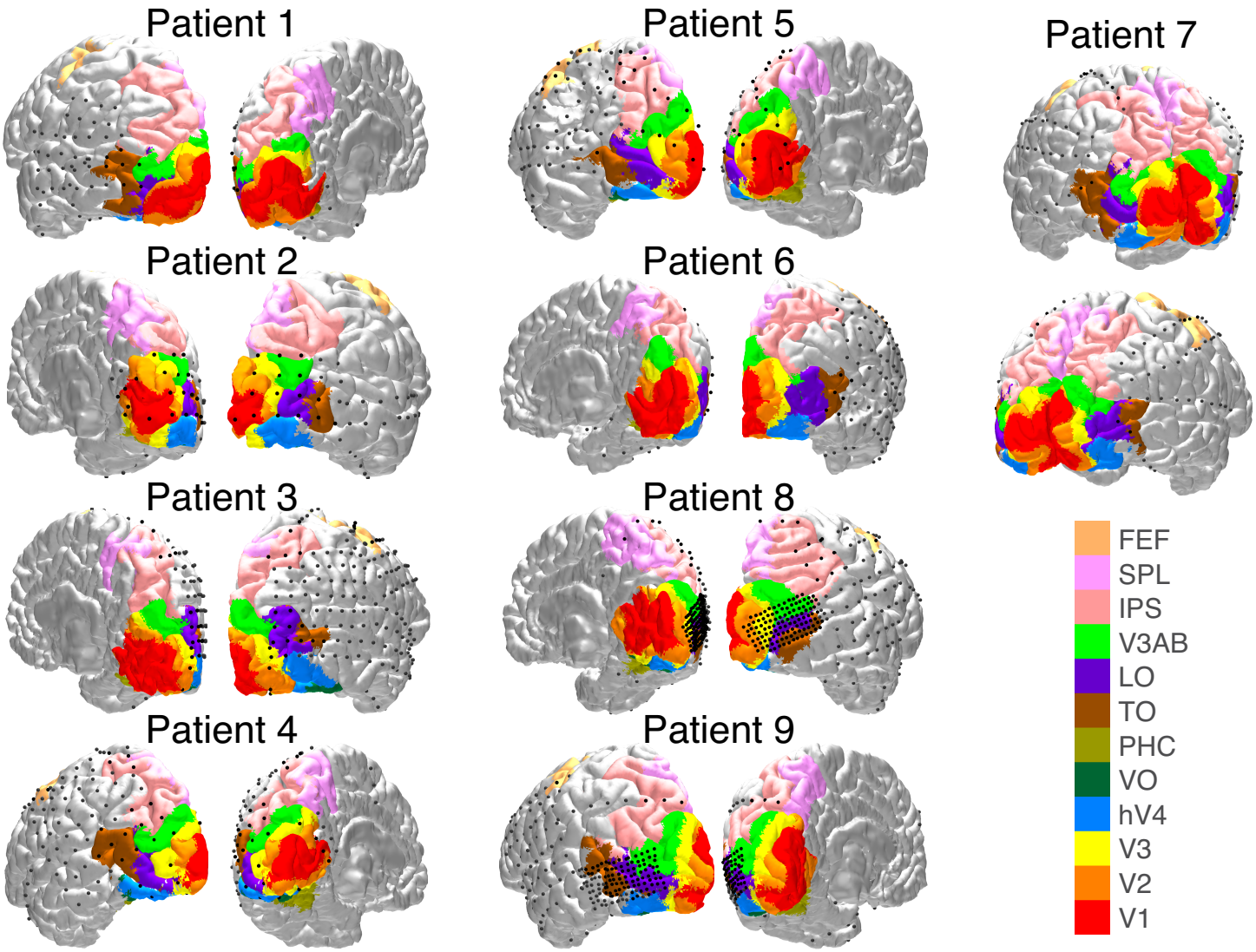

Supplementary Figure 1. Electrode locations and visual areas. The electrode locations and visual areas on brain surfaces for each patient. The retinotopic atlas is modified from Wang et al. [68]. Only the cortices with electrodes are shown: left cortex for Patient 1, 4, 5, and 9; right cortex for Patient 2, 3, 6, and 8; both cortices for Patient 7. See *makeFigureS1.m*

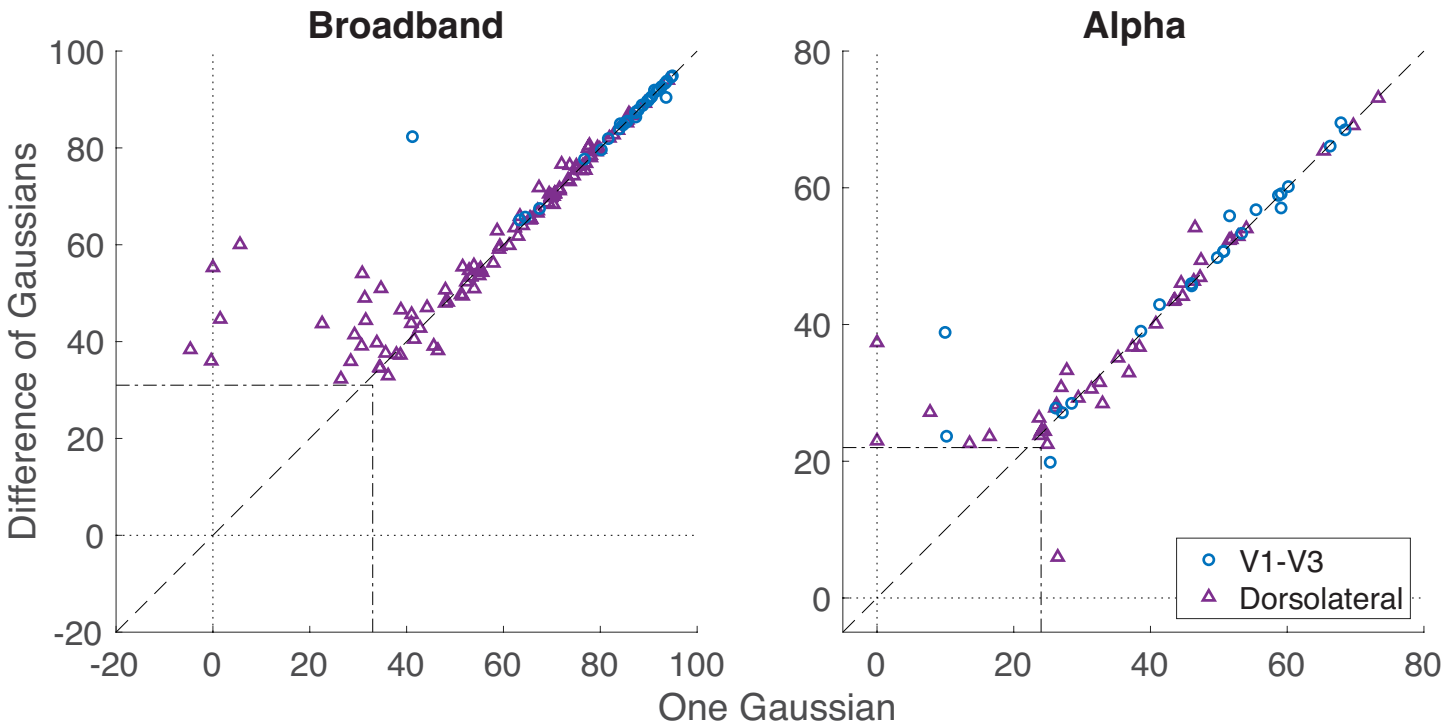

Supplementary Figure 2. PRF model comparisons between two Gaussian models. Cross-validated variance explained in pRF models are almost the same between two Gaussian models (Difference of Gaussians VS One Gaussian) both in V1–V3 (blue circle) and dorsolateral (purple triangle), but the Difference of Gaussians shows advantage in some electrodes. Each dot indicates electrode which is randomly selected according to the visual area probabilities in 5,000 bootstraps. See *makeFigureS2.m*

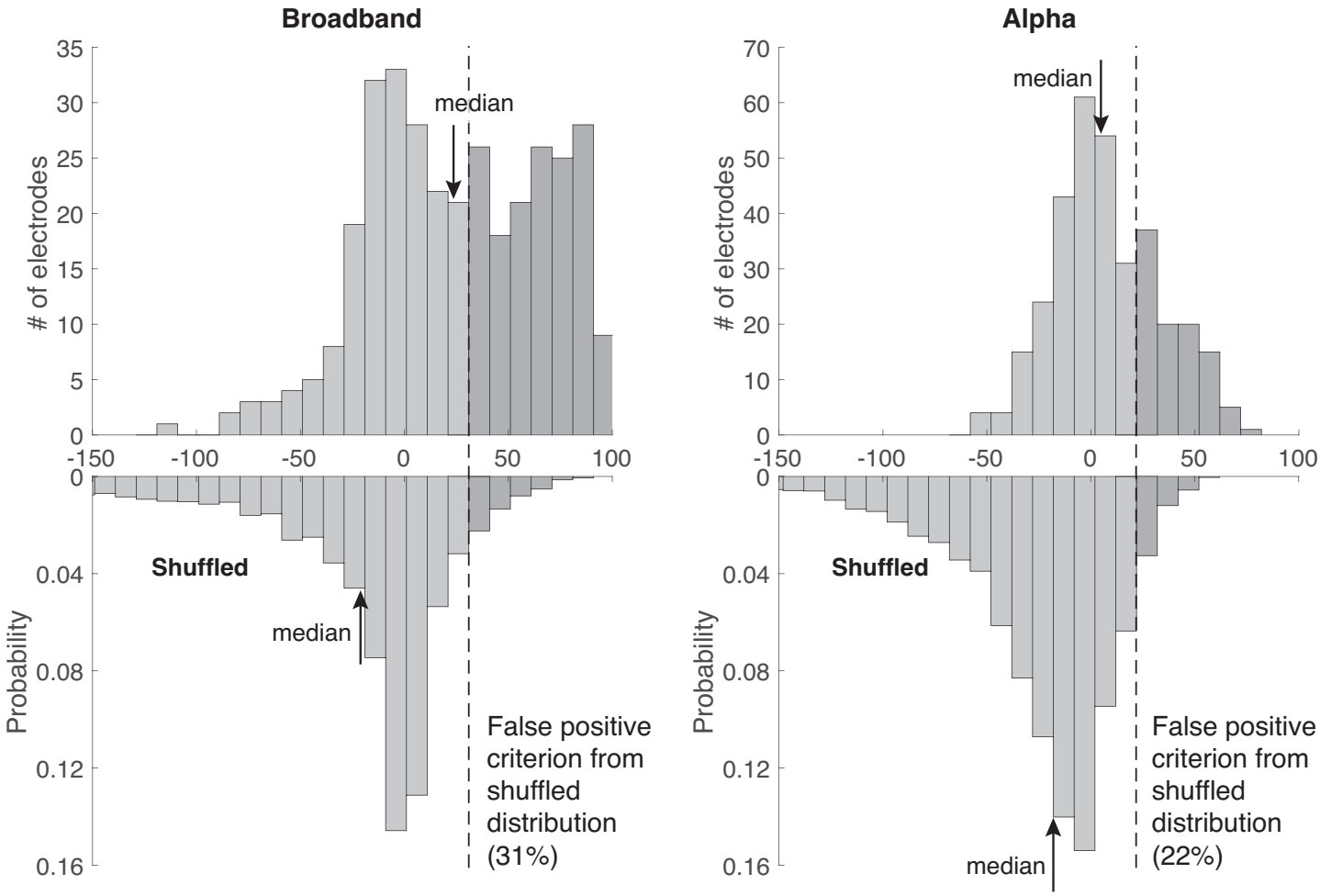

Supplementary Figure 3. Distributions of Variance Explained in alpha and broadband pRFs. The distributions of variance explained in alpha and broadband pRFs from all visual areas show rightward tendency compared to shuffled distributions. (A negative variance explained is common for cross-validation when making predictions with an inappropriate model.) The medians shown as black arrows have larger values in the raw distributions than the shuffled distributions (24% vs -21% in broadband and 5% vs -18% in alpha), suggesting the prediction accuracy of the pRF model fit is meaningful both in broadband and alpha. The false positive criterions were set at 95% of the values in this null distribution (dashed line: 31% for broadband and 22% for alpha). The electrodes shown in the right side of the false positive criterion (dark gray bars) were included for the comparison between broadband and alpha pRFs. in broadband pRFs are the visually selected electrodes. The electrodes shown in the right side of the false positive criterion in alpha pRFs are considered as the alpha sensitive electrodes. See *makeFigureS3_S4.m*.

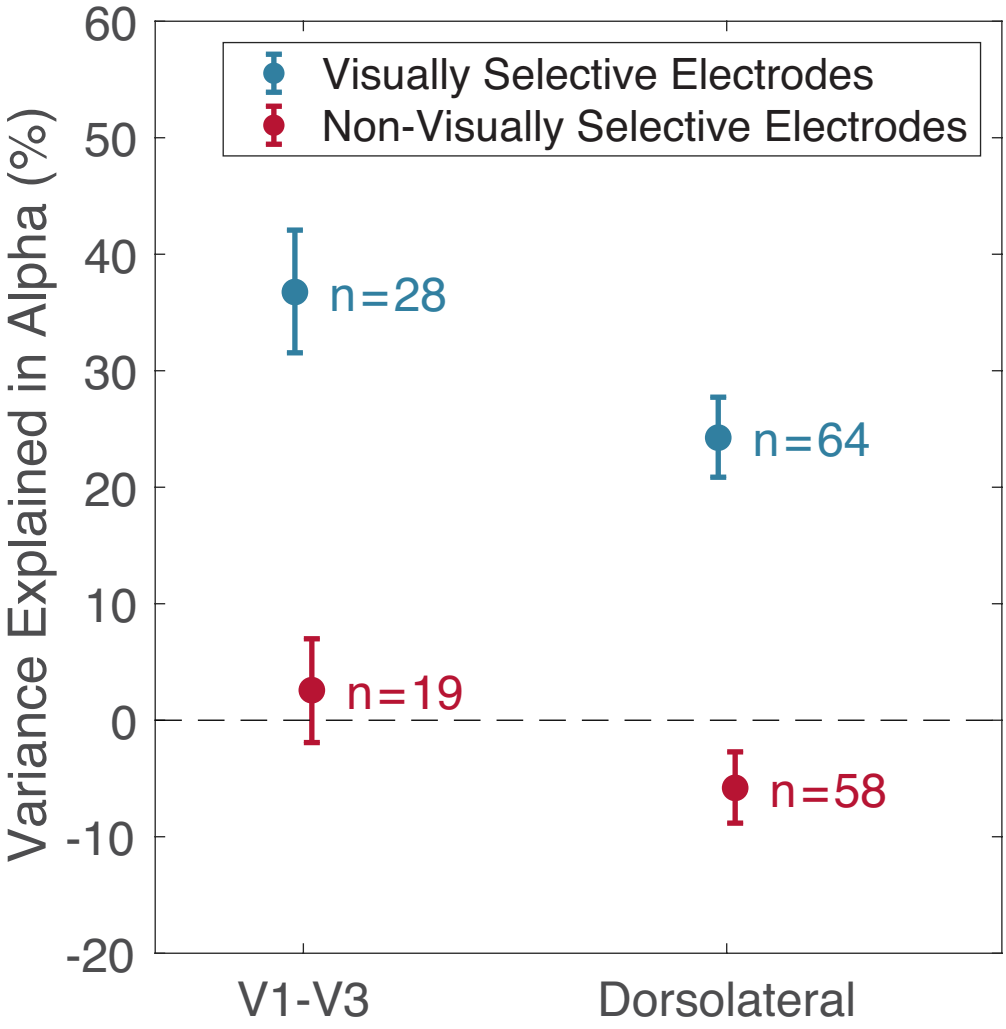

Supplementary Figure 4. Prediction accuracy of alpha pRF model. The average two-fold cross-validated variance explained of alpha pRF models was higher in the visually selective (blue) than in the non-selective electrodes (red) in V1–V3 and dorsolateral visual areas. Visually selective electrodes were defined as those whose broadband pRF model accurately predicted the broadband time course (see **Supplementary Figure 3**). Dorsolateral includes the V3A/B, LO-1/2, TO-1/2, and IPS maps. Electrodes were assigned to visual field maps probabilistically across 5,000 samples. Data points and error bars are means +/- 1 standard deviation of the mean across the 5000 samples. See *makeFigureS3_S4.m*.

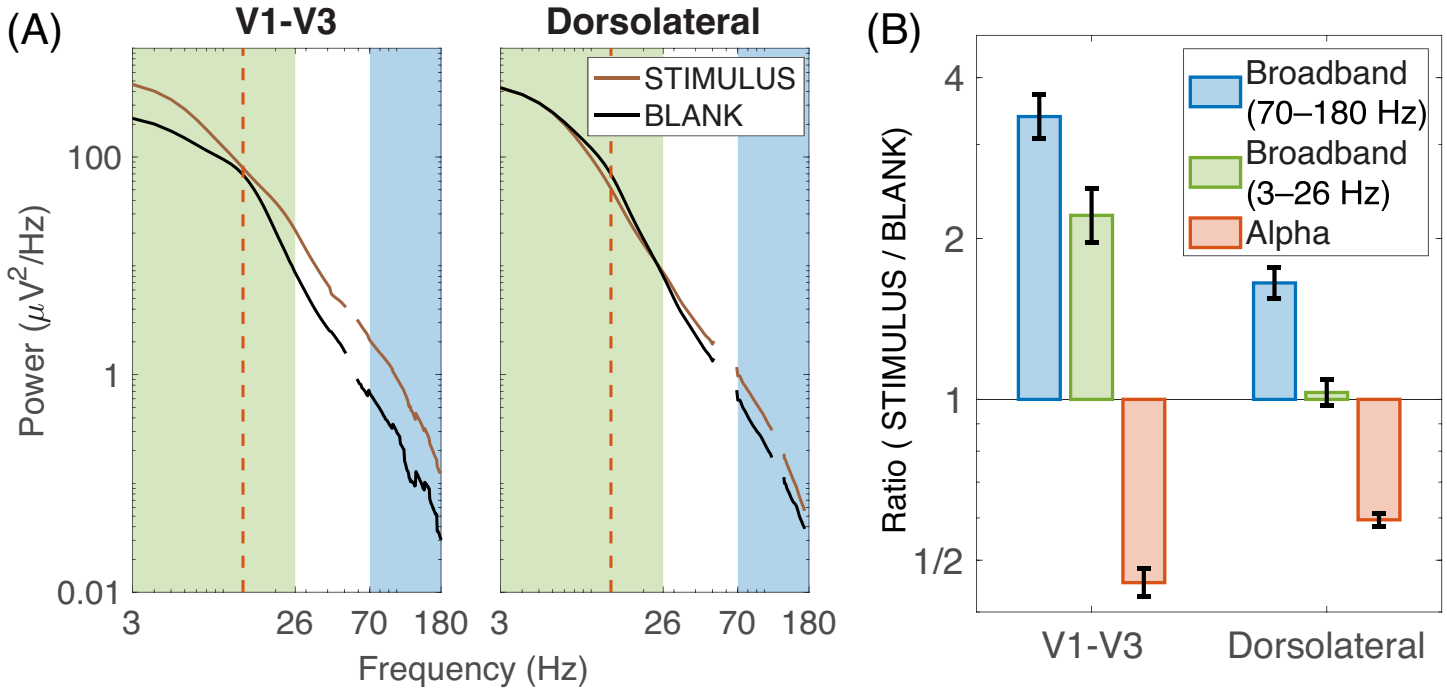

Supplementary Figure 5. Power in the broadband response and alpha oscillation. Each panel shows the spectral power changes averaged across all electrodes between BLANK and in-pRF stimulation (STIMULUS) conditions in V1–V3 and dorsolateral. (A) PSD for in-pRF (brown line) is higher than for BLANK (black line) and across all frequencies including not only high frequencies (blue region) but also low frequencies (green region) in V1–V3. In dorsolateral, on the other hand, PSD for in-pRF is higher than for BLANK only in high frequencies. Gaussian bumps at peak alpha frequencies (red dashed lines) are observed only in BLANK condition. (B) The ratio of PSDs between in-pRF and BLANK is positive in high-frequency broadband and negative at alpha frequency consistently in V1–V3 and dorsolateral. The ratio in low-frequency broadband is also positive in V1–V3 but is almost zero in dorsolateral. See *makeFigureS5.m*.

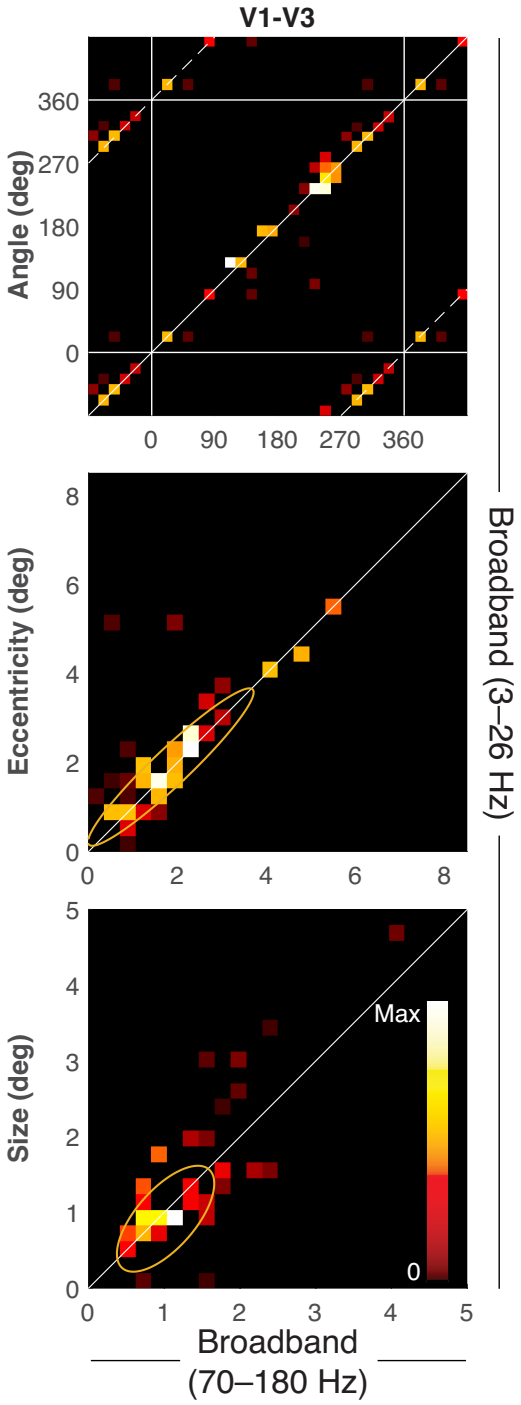

Supplementary Figure 6. Low broadband model comparisons. PRF parameters are highly correlated between the high-frequency broadband estimates (x-axis) and the low-frequency broadband estimates (y-axis) in V1–V3. Yellow ellipses indicate the 1-sd covariance ellipses. See *makeFigureS6.m*.

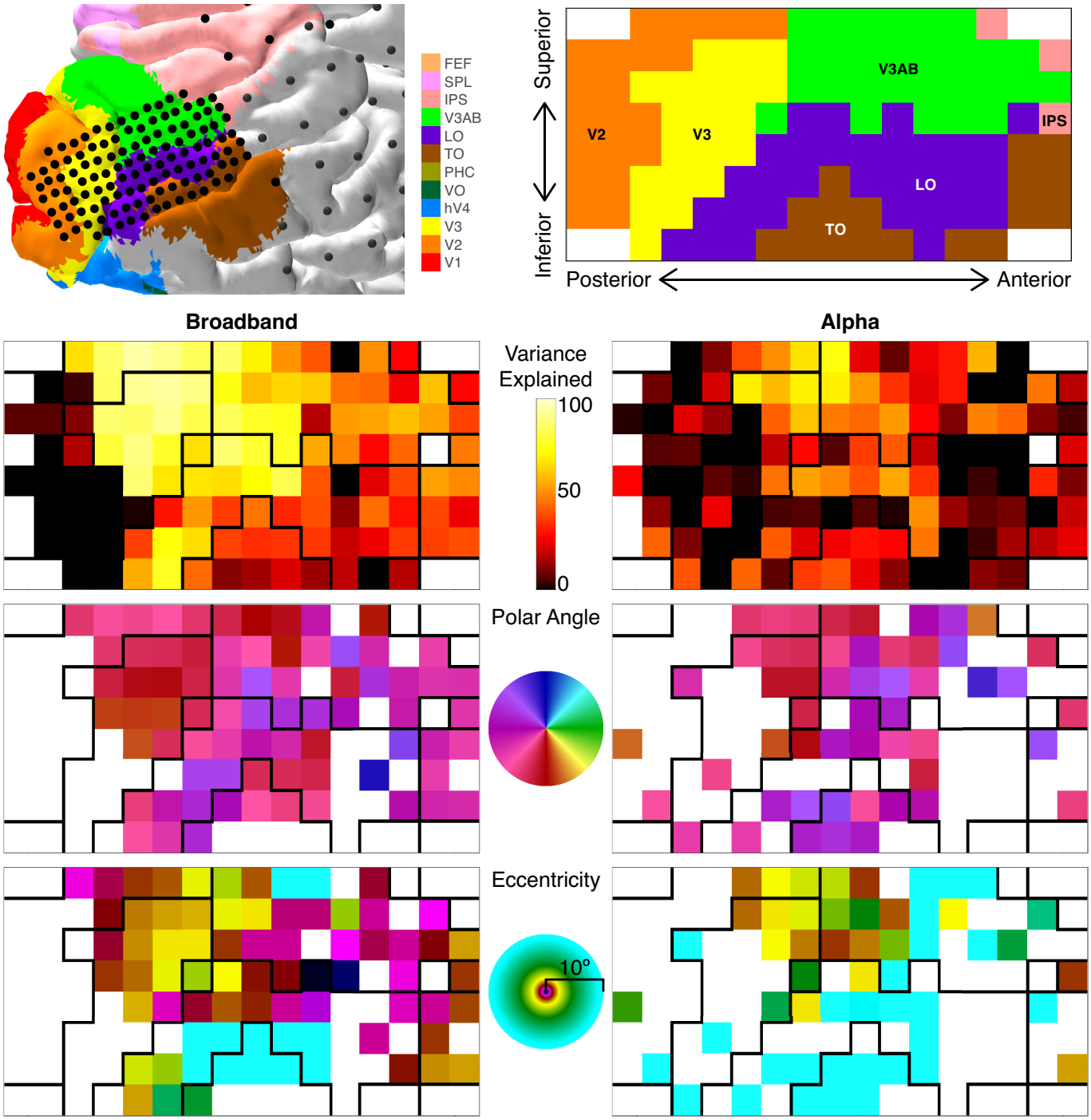

Supplementary Figure 7A. PRF parameters from high-density grid, Patient 8. (Upper left) The electrode locations and visual areas on the brain surface from Patient 8. (Upper right) The visual area assignments of electrodes from the high-density grid. White spaces indicate absence of electrodes. (Second row) Two-fold cross-validated variance explained in pRF fitting for broadband and alpha across electrodes in the high-density grid. Electrode locations which were excluded in the preprocessing are shown as white. (Third and Fourth rows) Polar angles and eccentricities of estimated pRFs. Electrodes which had low variance explained (under 31% and 22% for broadband and alpha, respectively) are shown as white. See *makeFigureS7.m*.

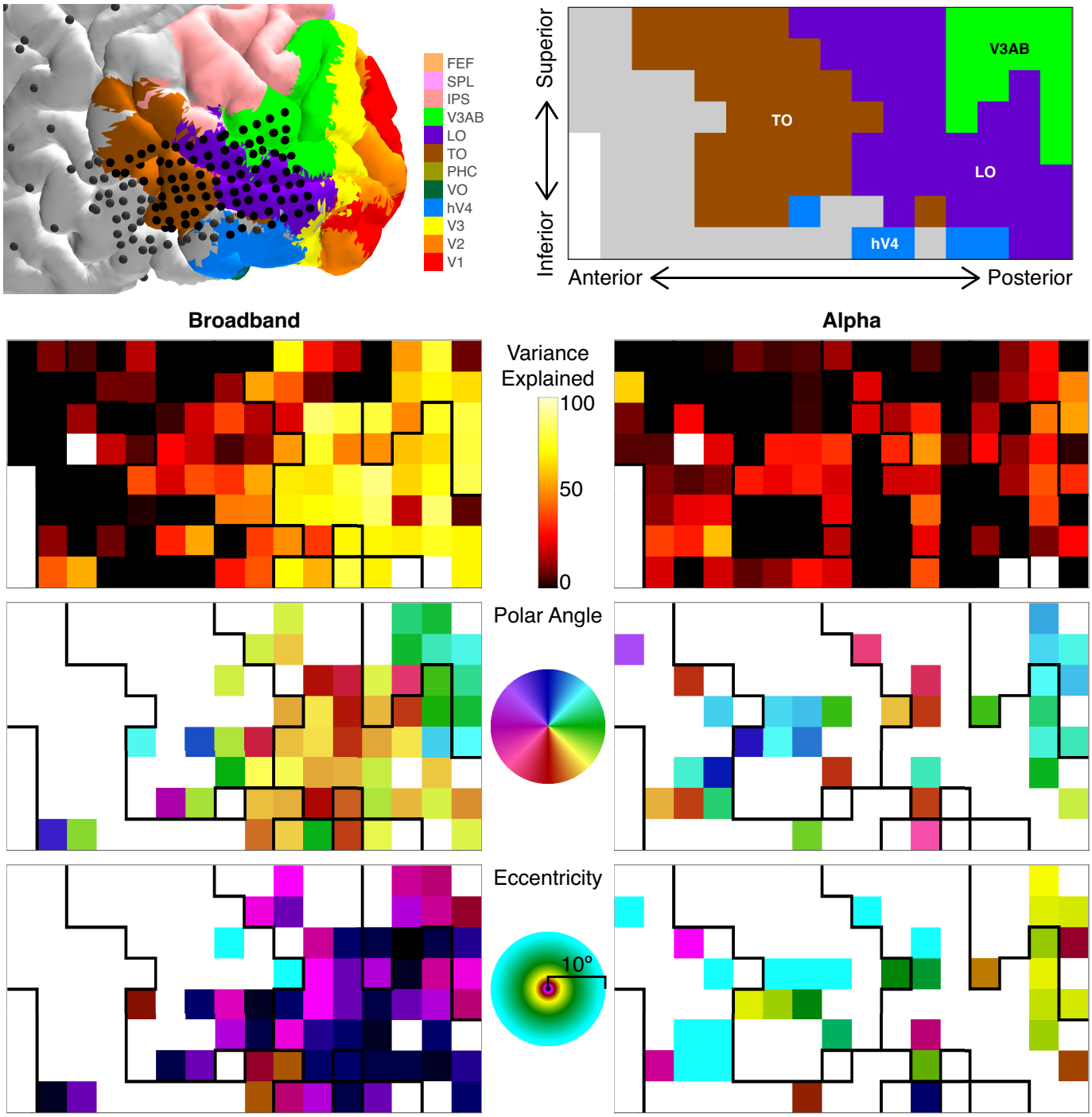

Supplementary Figure 7B. PRF parameters from high-density grid, Patient 9. (Upper left) The electrode locations and visual areas on the brain surface from Patient 9. (Upper right) The visual area assignments of electrodes from the high-density grid. White spaces indicate absence of electrodes. Gray spaces indicate electrodes which were not assigned to any visual areas. (Second row) Two-fold cross-validated variance explained in pRF fitting for broadband and alpha across electrodes in the high-density grid. Electrode locations which were excluded in the preprocessing are shown as white. (Third and Fourth rows) Polar angles and eccentricities of estimated pRFs. Electrodes which had low variance explained (under 31% and 22% for broadband and alpha, respectively) are shown as white. See *makeFigureS7.m*.

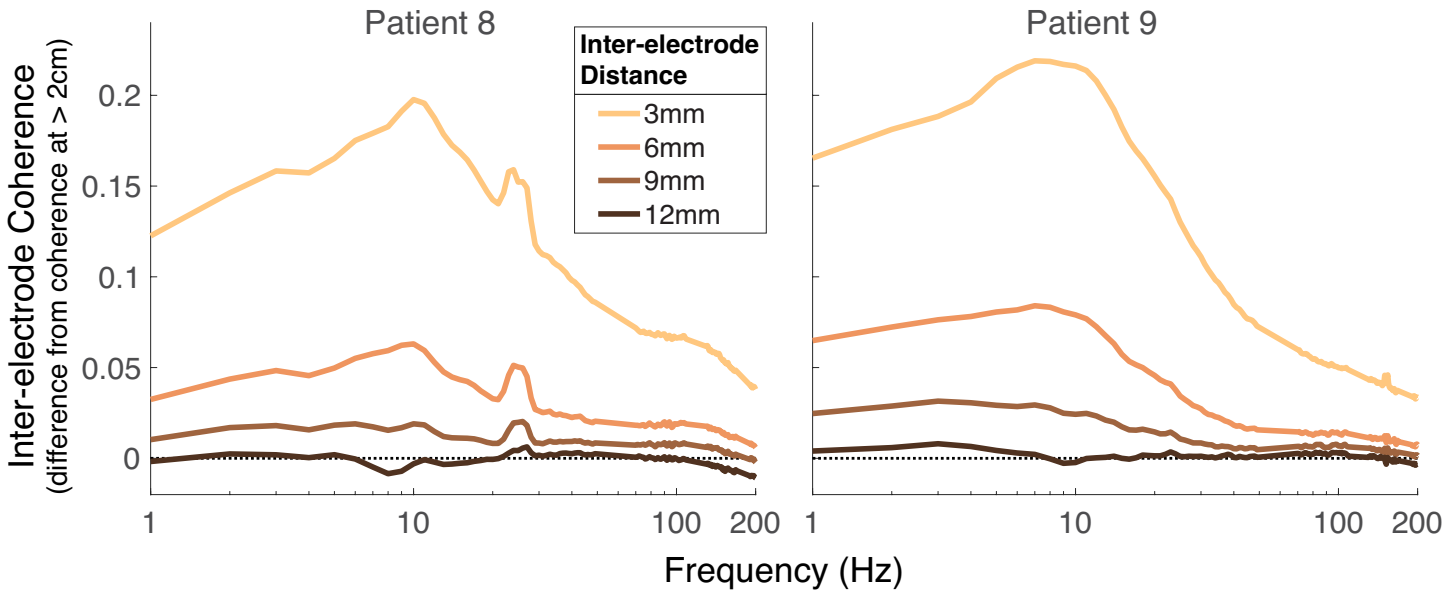

Supplementary Figure 8. Inter-electrode coherence in the high-density grids across 1–200 Hz. Each curve indicates the coherence averaged across electrode-pairs, binned by inter-electrode distance. The coherence for electrode pairs more than 2 cm apart was used as a baseline, and subtracted from each curve. For both patients, the coherence is highest around 10 Hz, the frequency of the alpha oscillation. See *makeFigureS8.m*.

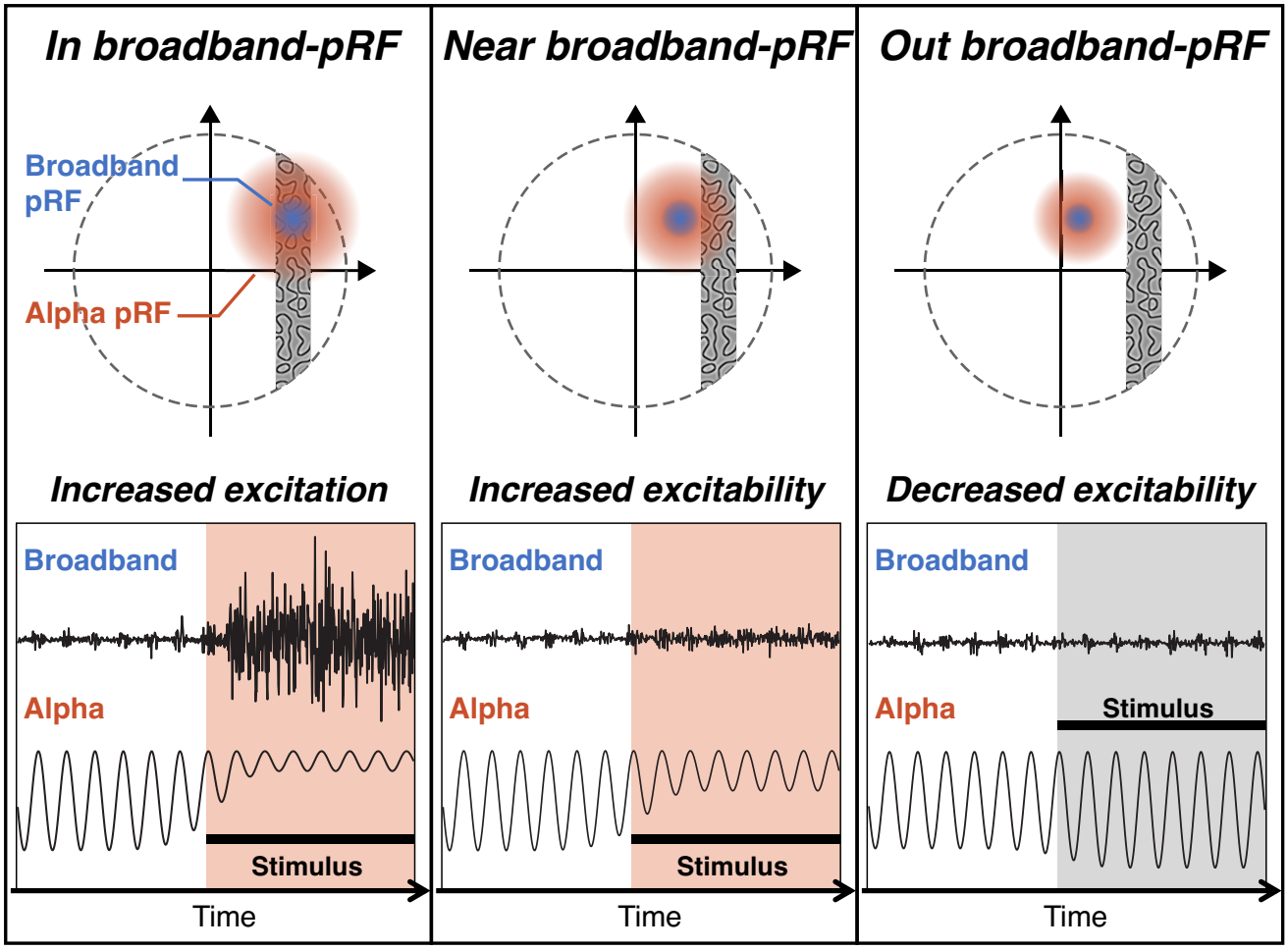

Supplementary Figure 9. Schematics of neural excitation and excitability changes induced by visual stimulation. The upper panels show stimulus position relative to the broadband and alpha pRFs for a given electrode. The lower panel shows predicted alpha and neural responses from that electrode, with stimulus onset indicated by the black horizontal bar. In the left and right panels, stimulus onset causes the alpha oscillations to be suppressed and cortex to become more excitable (red shading). In the right panel, the alpha oscillation increases slightly and cortex becomes less excitable (gray shading).

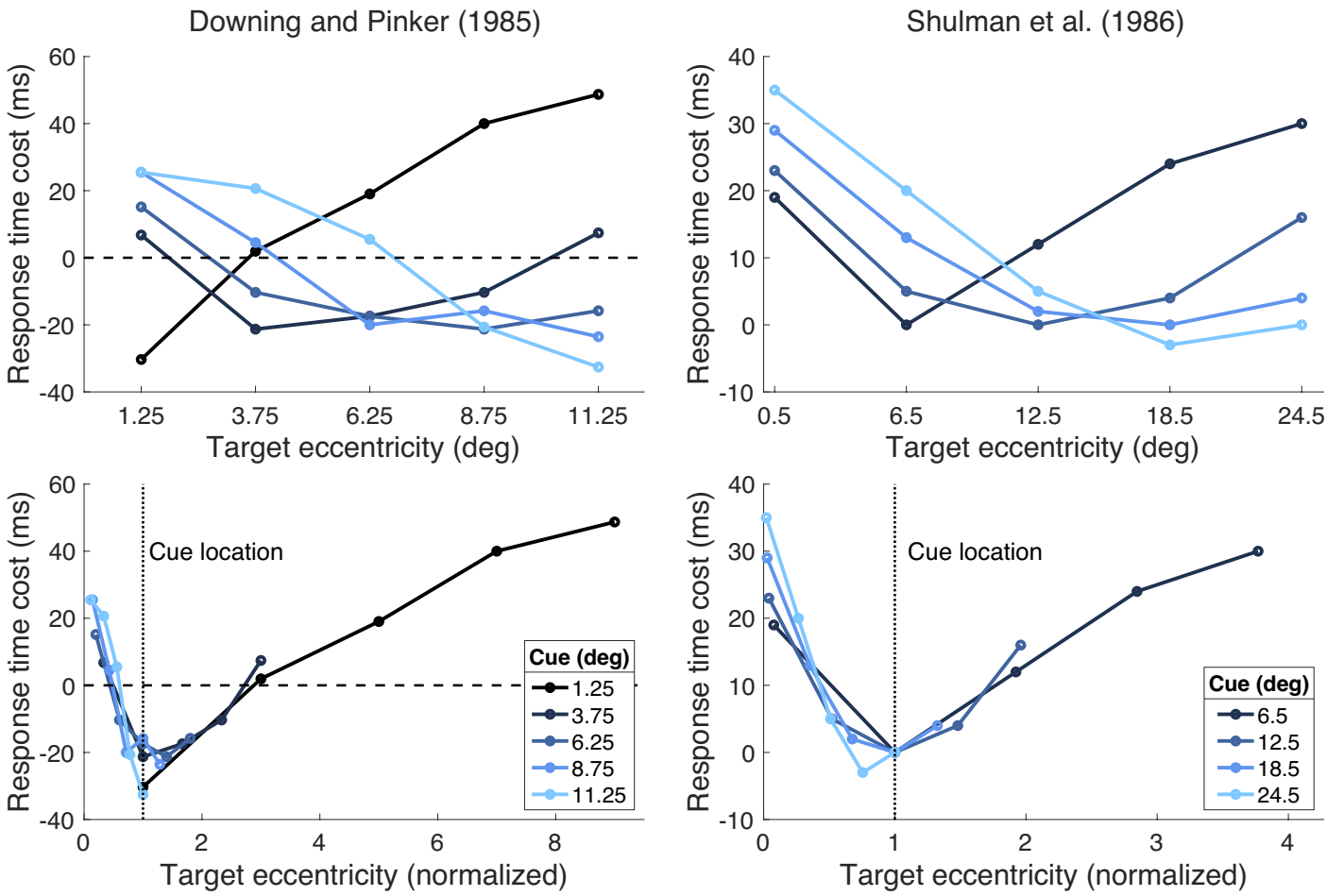

Supplementary Figure 10. Response time costs in previous exogenous attention experiments. Left panels represent response time changes induced by exogenous attention from Downing and Pinker [30], relative to the response time without any attentional cue. Right panels represent response time changes induced by exogenous attention from Shulman et al. [29], relative to the response time when targets appeared at the attended locations. Lower panels are the same results as top panels after normalizing target eccentricities by dividing by the cue eccentricities. Results from the Shulman et al. paper with foveal cue locations at 0.5 degree eccentricity were excluded from the plot because after normalizing, the data from this condition has no overlap with the other conditions. See *makeFigureS10.m*.

REFERENCES

29. Shulman, G.L., Sheehy, J.B. & Wilson, J. Gradients of spatial attention. *Acta Psychol (Amst)* **61**, 167-181 (1986).
30. Downing, C.J. & Pinker, S. The spatial structure of visual attention. in *Mechanisms of attention: Attention and performance XI* 171-187 (1985).
68. Wang, L., Mruczek, R.E., Arcaro, M.J. & Kastner, S. Probabilistic Maps of Visual Topography in Human Cortex. *Cereb Cortex* **25**, 3911-3931 (2015).